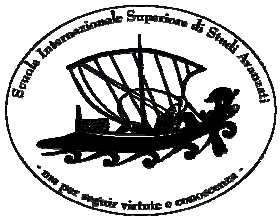

Scuola Internazionale Superiore di Studi Avanzati, Trieste, Italy

Theoretical Studies on the KcsA Potassium Channel

Thesis submitted for the degree of

Doctor Philosophiæ

Candidate:

Leonardo Guidoni

Supervisors:

Dr. Paolo Carloni

Prof. Vincent Torre

October 2000

To Silvia

TABLE OF CONTENTS

Introduction

Ionic channels are proteins forming pores through cell membrane allowing cells to exchange ions with the external environment. Ionic fluxes regulate a vast variety of vital processes in organisms from bacteria to mammalians, among which the muscle contraction and the nervous signal transmission [1].

Potassium channels are a large sub-family of ionic channels. They possess the capability to be highly selective of K^+ over Na^+ ions and other ionized particles. The strong ability in selectivity is accompanied to speed and a high ionic throughput. As a result, channel proteins are the fastest biological devices: a single channel, forming a tunnel across the cell membrane, is able to process up to 10^8 ions per second. Ion permeation is driven by electrostatic potential difference between internal and external sides of the membrane [1-4].

The ion permeation is believed to occur in several steps [1]. First, the ions diffuse from the cytoplasm (or extracellular) solution towards the protein channel mouth. The binding to the channel pore is accompanied by partial or full dehydration. Subsequently, the ions translocate through the pore (the narrowest part of the channel). Finally, the ions reacquire their hydration shell on the other side of the protein. The total ion pathway is rather short (~4 nm). Experimental evidence indicates that K^+ channels contain multi-ion pores, namely few ions are simultaneously present inside the channel [5].

During the permeation process, the ions may encounter energy barriers (for instance between two pore binding sites). Deciphering the location and the energetics of these barriers is therefore a key step to understand the mechanisms of ion transport. In particular it is unknown whether the rate-limiting step is the dehydration process or the translocation movements into the pore region. The physical origin of ionic selectivity

may be revealed by the identification of specific free energy barriers governing the K^+ recognition at the molecular level.

K^+ channels, as other membrane proteins, are difficult to crystallize [6]. Up to few years ago, no X-ray structure was available. Theoretical studies, limited to peptide channel models (as gramicidin A) suggested that the time course for water ligand substitution might acts as a major barrier retarding ion transport [7]. The idea that the rate-limiting step is due to ion dehydration was transferred to K^+ channels and represented the current view on potassium transport [1].

In 1998, the availability of the 3D structure of a K^+ channel [8] opened the avenue to understand the physical mechanisms regulating ionic transport, binding, and selectivity in a selective ionic channel. The structure reveals that permeating ions pass through a funnel so narrow that ion dehydration is required. This small pore is the part of the protein totally responsible for selectivity, although it represents only about one third of the full ion pathway across the membrane.

This thesis started with the publication of this seminal paper. We have applied a variety of computational tools, as molecular dynamics (MD) and electronic structure calculations based on density functional theory (DFT), to study the molecular mechanisms of the ionic permeation, selectivity, and binding. Using a molecular model of the channel embedded in a membrane mimic environment, we have investigated functional and dynamical properties of the channel, taking into account the full complexity of the protein, ions and water interactions. During the development of the thesis further structural information, based on electronic paramagnetic resonance (EPR), has also provided complementary data to the X-ray investigation [9,10].

Four main issues are addressed by the present study:

1. The validity of our computational setup and of our molecular model are tested in comparison with the X-ray data itself, EPR studies and available electrophysiological experiments. The fundamental interactions responsible for protein and ion stability are investigated.
2. We study fundamental aspects of energy barriers during ion permeation. In particular we focus on the dehydration step, to investigate whether it is (like usually assumed [1]) the rate-limiting barrier. The dehydration process from the

bulk solution to the binding sites can be followed for both K^+ and Na^+ ions. We also investigate the role of hydration in ionic selectivity.

3. Confined water inside narrow pores has been extensively studied and differs that in the bulk by physical properties [11]. The behavior of the water in the K^+ channel should be investigated to understand if it could play some role in the transport process. We study the water dynamical properties into the channel with the intent to establish if they would have some functional role in the ion permeation.
4. We describe in detail the changes of the coordination chemistry and of the chemical bonding associated to ion translocation through the selectivity filter. This study can reveal fundamental aspects of the energy barriers in this permeation step.

The first chapter introduces to the biological problem and to the open issues on K^+ channels, summarizing the available structural data and the current theoretical standpoint. Methods and details about the structural model and the computational procedures used in our calculation are given in chapter 2 and 3, respectively. Results are reported in chapter 4 and compared to experiments. A comparison with other molecular dynamics simulations that appeared during and after our works is also discussed at the end of the chapter (§ 4.6). Finally, we summarize our findings and suggest future perspectives.

1 Structure and function of K^+ channels

In the first two paragraphs, a general introduction to the cell membrane and to ionic channels will be given. We will first focus on the general features of K^+ channel (§ 1.3), than we will describe in details the functional (§ 1.4.1) and structural characteristics (§1.4.2-3) of the KcsA channel from *Streptomyces lividans*, of which the X-ray structure has been recently solved [8]. We will summarize in § 1.5 the theoretical approaches developed on the most relevant issues of these systems. Finally, we will outline the aim of the present work (§ 1.6).

1.1 The cell membrane

Evolution built a membrane around the earliest forms of life in order to isolate them from the external environment. The cell membrane is constituted by two layers of phospholipids, held together by noncovalent interactions (Fig. 1.1A,B). These molecules are characterized by having a hydrophilic polar head and hydrophobic non-polar tails (Fig. 1.1C). The two films of these molecules are therefore assembled together by hydrophobic forces forming a lipid bilayer ~ 5 nm thick around the cell that is stable in aqueous environment [12,13].

Membrane proteins are inserted in this amphiphilic environment, having both hydrophobic and hydrophilic regions on their surface (Fig. 1.1B). The protein mass on the cell surface represents a significant part of the membrane, ranging from ¼ to ¾ of the total membrane mass [12]. In highly evolved and specified cells this class of proteins carries out a variety of different activities essential for the cell and organism life, such as the antibody recognition in lymphocytes and the nervous pulse transmission in neurons.

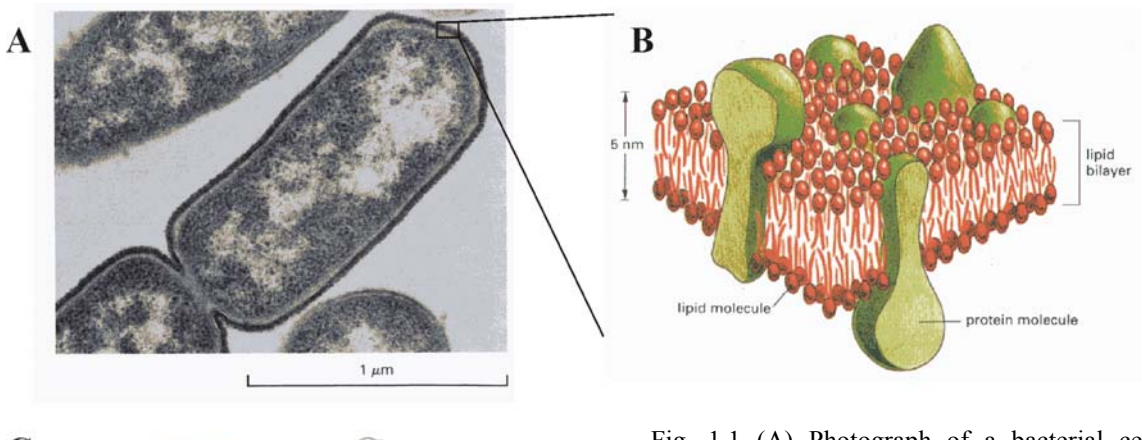

Fig. 1.1 (A) Photograph of a bacterial cell taken through an electron microscope (figure adopted from ref. [13]). (B) Diagram of a plasma membrane patch. Membrane proteins (green) are inserted in the phospholipid bilayer (red). Figure adopted from ref. [12]. (C) Chemical sketch (left) and van der Waals representation (right) of a single phosphatidylcholine phospholipid molecule (figure adopted from ref. [12]).

The three dimensional atomic structure of the majority of the membrane proteins is still unknown because of the difficulties in extending to this class of proteins standard tools like X-ray scattering on molecular crystals. Membrane proteins are indeed difficult to crystallize because they are not soluble in water and they denature in organic solvents [6]. Furthermore, the difficulties in finding host organisms for high-level gene expressions are much larger than those encountered for globular protein expression. For these reasons, although genes encoding for membrane proteins are supposed to be one third of the total genes, only ~ 0.2 % of the known biological macromolecular structures to date belongs to this class of proteins.

Although the presence of the membrane helps cells to retain vital ingredients, it prevents access to the necessary ionized substrates and ions, because the hydrophobic core is a high free energy barrier in the diffusion of charged molecules.

Ionic channels are a class of membrane proteins, which form holes through the cell membrane, providing a feasible path for ion exchange.

1.2 Ionic channels

Ionic channels are proteins inserted in the membrane lipid bilayer as shown in the cartoon of Fig.1.2 by forming aqueous pores through the cell membrane [1,2]. They allow ions to cross the hydrophobic barrier of the core membrane, guaranteeing to the cell a controlled exchange of ionized particles.

In resting conditions the internal side of a cell has a lower electric potential than the external side [1]. When ions flux through the channels, they produce an electric current accompanied by changes of the membrane potential[1].

Ion permeation is crucial for a variety of biological functions such as nervous signal transmission and osmotic regulation [1].

The open state of these proteins may be regulated by a variety of factors that open and close the channel mouth allowing and preventing the ionic flux. Indeed, the gating mechanisms can be based on chemical-physical properties like the membrane potential (voltage gated channels[3]), pressure-induced structural changes (mechanosensitive channels [14]), ligand binding (such as cyclic nucleotides activated channels [15]) or pH variations (such as KcsA potassium channel [16,17]).

An important property of channel in the open state is given by their selective permeability. This is defined as the ability to allow only a restricted class of ions to flow trough the channel pore in large amounts. Channels may require permeating only ions

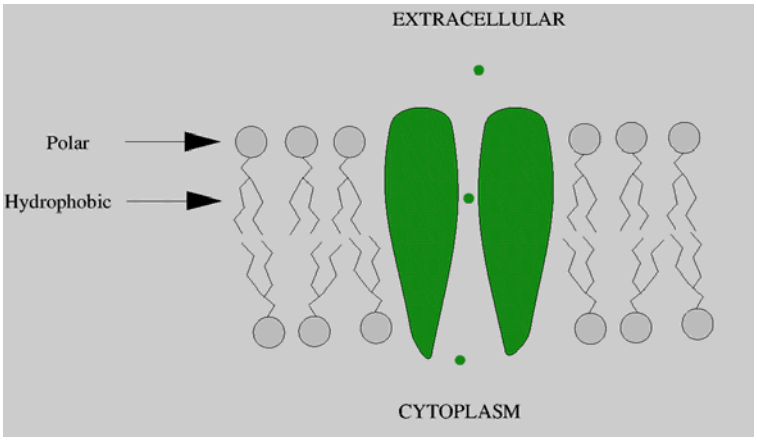

Fig.1.2 Schematic representation of ions (green dots) flowing trough an ionic channel (green cartoon) embedded in the phospholipid bilayer of the cell membrane (gray sketches).

[1] The membrane potential is defined as the difference between the electrostatic potential inside the cell and that outside the cell.

with a specific charge, thereby selecting anions over cations like in chloride channels [18,19], or selecting divalent cations over monovalent cations like in calcium channels [1,2]. Ionic selectivity is commonly measured by patch clamp techniques using biionic conditions, namely bathing the outer (o) and inner (i) membrane sides with solutions containing different ionic species A, B. In these conditions, the applied potential E_{rev} (the reversal potential) needed to observe zero current flow can be measured. E_{rev} defines the permeability ratio P_A/P_B between the two species through the equation:

$$E_{rev} = \frac{RT}{zF} \ln \frac{P_A[A]_o}{P_B[B]_i},$$

where z is the ionic valence, RT the Boltzmann factor, and F the Faraday constant [1].

A deep understanding of these properties can help to rationalize several diseases associated with defects in ionic channel function, the majority of them arising from mutations of the genes encoding the channel proteins. Large effort is still required to connect these mutations to the structural and functional changes affecting these pathologies [20].

In summary, ionic channels differ in functional, gating and selectivity properties. They are accommodates in a large variety of cells. Hereafter we focus on a specific class: the voltage gated K^+ channels. This class plays a crucial role in many fundamental biological events, such as the nervous signal transmission in neurons.

1.3 Voltage-gated K^+ channels

A nervous pulse is an electrical signal produced by the ionic flux trough the plasmatic membrane of a neuronal cell. Each neuron receives the electric synaptic inputs from dendrites around the cell body and transmits the signal to other cells through a long and branched termination (the axon). In cells the intracellular K^+ concentration is much higher than that of Na^+. ATP-based active transporters maintain these gradient concentrations, pumping ions against their electrochemical gradient [21]. In the absence of a signal, the membrane potential, is ~ -60 mV and the membrane is mainly permeable to K^+ ions. During signal transmission, the membrane polarization changes,

assuming positive values (~ 30mV) and subsequently coming back to the resting potential. This pulse, the action potential, propagates along the axon as a 'potential wave'. Cole and Curtis [22] found that these changes in membrane potential are tightly linked to changes in the membrane impedance.

In 1952 Hodgkin and Huxley [23], through a mathematical formalism describing the membrane current of the squid giant axon, demonstrated that the Na^+ and K^+ membrane permeabilities change during the action potential. The total current may be separated into two different contributions from Na^+ and K^+ ionic fluxes. Potassium and sodium follow different routes when crossing the membrane, using high selective channels, which open and close as a function of the membrane potential. The interplay between these two contributions leads to the propagation of the nervous signal along the axon[2].

K^+ channels are highly selective proteins; in particular, they are more selective than Ca^+ or Na^+ channels. Typical values for the P_{Na^+}/P_{K^+} permeability ratios are in the range 0.01-0.1 [1].

The first potassium channel gene was cloned in 1987 from fruit fly *Drosophila* (the *Shaker* gene) [24]. The *Shaker* channel became a paradigm of the voltage gated K^+ channels. It opened the avenue to the discovery of other K^+ channel genes [25] and started the combined use of sequence manipulation with patch clamp techniques [26-30].

The primary structure of the gene revealed the presence of one cluster of putative membrane-spanning segments. The overall structure of the K^+ channel has been found

Fig. 1.3 Membrane topology of voltage gated potassium channels.

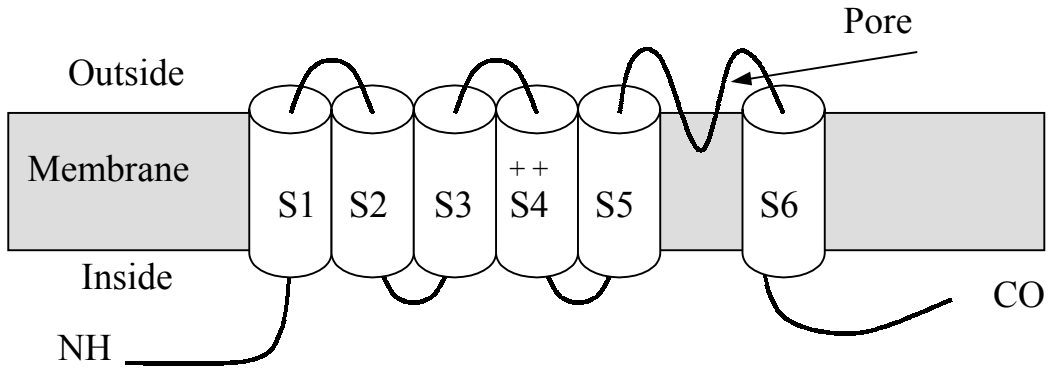

[2] Note that during this process, although the membrane potential undergoes large variations only a small fraction of the alkali ions (~ 0.001 %) passes through the plasma membrane.

to be tetrameric [31], formed by four identical subunits assembled together around the channel pore. In most cases each subunit is formed by six transmembrane (TM) helices (Fig. 1.3); the protein is therefore constituted by a bundle of 24 helices.

The S4 helix (Fig. 1.3) is responsible for the voltage dependence of the channel, and contains a highly conserved sequence of positively charged amino acids. This voltage sensor regulates the channel conductivity as a function of the membrane potential, and similar structures are also common features in Ca^+ and Na^+ voltage-gated channels.

The pore region (about 30 amino acids) is located between S5 and S6 (Fig. 1.3). The selectivity filter is responsible for potassium selectivity, consisting of a sequence of five highly conserved residues located in the middle of the pore region (Fig. 1.4). Modification of these conserved amino acids leads to strong alteration or destruction of the potassium selectivity [27,29].

The selectivity filter was supposed to be the narrowest part of the channel pore, through which ions need to flow during permeation. Ion was postulated to be a multi-ion process [32]. The presence of few ions in the narrow selectivity filter results in the requirement that the ionic flux needs to occur in a concerted, single-file motion [5], as there is no space for two ions to exchange positions without exiting the pore.

The multi-ion nature of a channel is also reflected in the concentration dependent permeability ratios. In biionic conditions, indeed, a flux-coupling situation occurs where there is a strong dependence of the two different ionic fluxes on each other. In these conditions the permeability ratios depends on the ionic concentrations in a non-linear way, generating the so-called anomalous mole-fraction dependence [33].

1.4 The KcsA channel

Bacterial genomes show sequences that are homologues to eukaryotic potassium channels [16,34,35]. However, the physiological role of these prokaryotic genes is still at the level of speculation (for a review see ref. [4]). In 1995 the cloning [16] of the first bacterial gene encoding for a potassium selective channels (the *KcsA* gene) opened the avenue to large-scale production of purified K^+ channels, and led in 1998 to the *KcsA* channel crystallization and the determination of its 3D structure [8]. After the KcsA

gene from *Streptomyces lividans* was cloned [16], mM quantities of bacterial channels have been purified and successfully reconstructed in detergent micelles for functional studies [16,17,36-38].

In this section, after having summarized the general features of the KcsA bacterial channel, we describe the crystal structure. We mention also EPR studies that had provided structural information complementary to the X-ray work [9,10].

1.4.1 General Properties: opening and blocking the channel

Opening of the channel. Single channel measurements on reconstructed proteins incorporated into lipid bilayers revealed a strong pH dependence of the channel opening probability [17]. High proton concentration (pH <5.0) promotes channel opening, while in neutral conditions no significant single channel activity was observed. Recent investigations have suggested that the protonation site responsible for channel opening is located in the intracellular side [39], despite previous works supposing an extracellular gating site [9,17,40]. The channel exhibits K^+ selectivity over Na^+ and other cations. The measured permeability ratio P_{Na^+}/P_{K^+} exhibits a moderate selectivity: 0.35 [16], 0.1 [38], 0.09 ± 0.01 [41] (see also ref. [17]). Because of the difficulties of such measurements, and the complication od subconductance levels [41], it is difficult to attribute to them a definitive value [38].

Channel inhibitors. Common blockers, such as Ba^{2+}, tetraethylammonium (TEA) and toxins [1] inhibit the current through the KcsA channel as happens for all the other K^+ channels[41]. In particular, cytoplasmic Ba^{2+} [38] and application of TEA to either side of the membrane [17] dramatically reduced the ion flux in μM and mM concentrations respectively[39,41]. Peptide toxins present in scorpion venom are K^+ channel inhibitors interacting strongly with specific sites at the extracellular mouth of the protein, obstructing the pore and blocking ion transport. Using site directed mutagenesis on the bacterial channel it has been possible to make a KcsA mutant sensible to a *Shaker*-acting toxin [42], thereby showing the structural conservation between prokaryotic and eukaryotic channels [43].

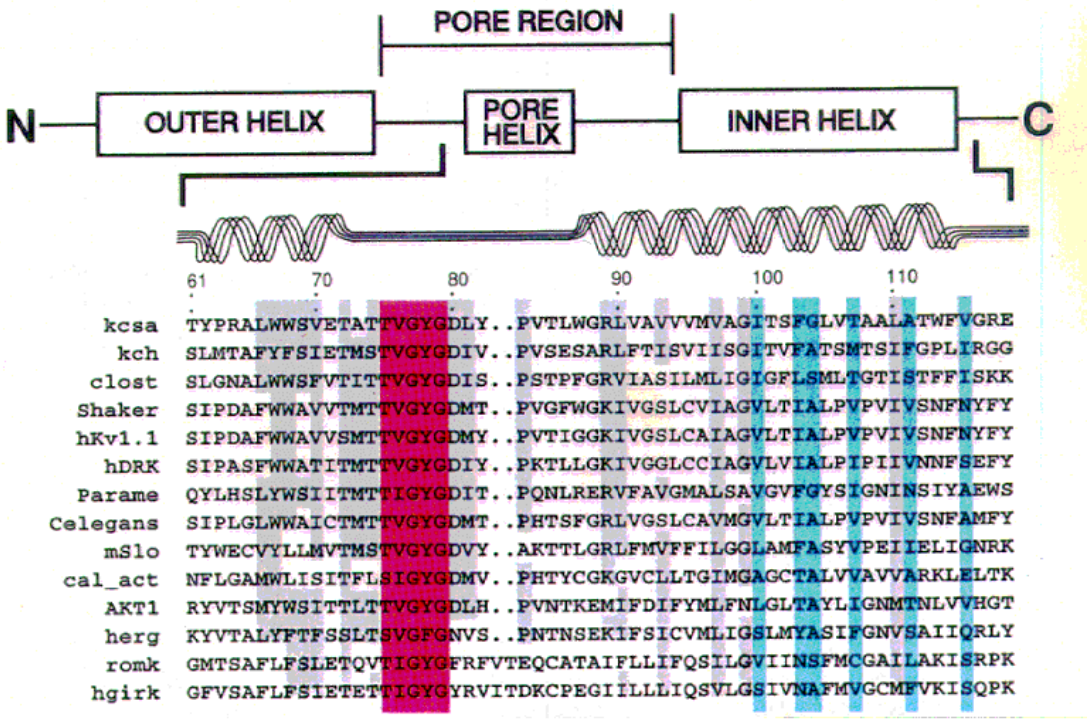

Fig. 1.4. Sequence alignment of the K^+ channel family. Figure adopted from ref. [8].

The KcsA channel is smaller than the eukaryotic analogues. It has only two transmembrane helices as oppose of six in voltage gated K^+ channels, namely the S5 and S6 helices of Fig. 1.3. The overall pore region sequence shows a large similarity to the potassium channel family (Fig. 1.4), and, in particular, it has the same selectivity filter sequence fingerprint (TVGYG) of al K^+ channels. Despite the smaller dimensions, the protein is still able to preserve pore properties like permeation, blocking and selectivity close to these of larger K^+ channels. Thus, it is an optimal candidate for structural studies.

1.4.2 The structure

The KcsA potassium channel is formed by four identical subunits, each composed of 158 residues, of which 97 are detected in the crystallographic structure [35].

The structure is shown in Fig. 1.5. In panel A, the full structure is represented by sticks using standard color mapping: C (light blue), N (dark blue), O (red), and S (yellow). Two rings of aromatic residues characterize the membrane/water interfaces

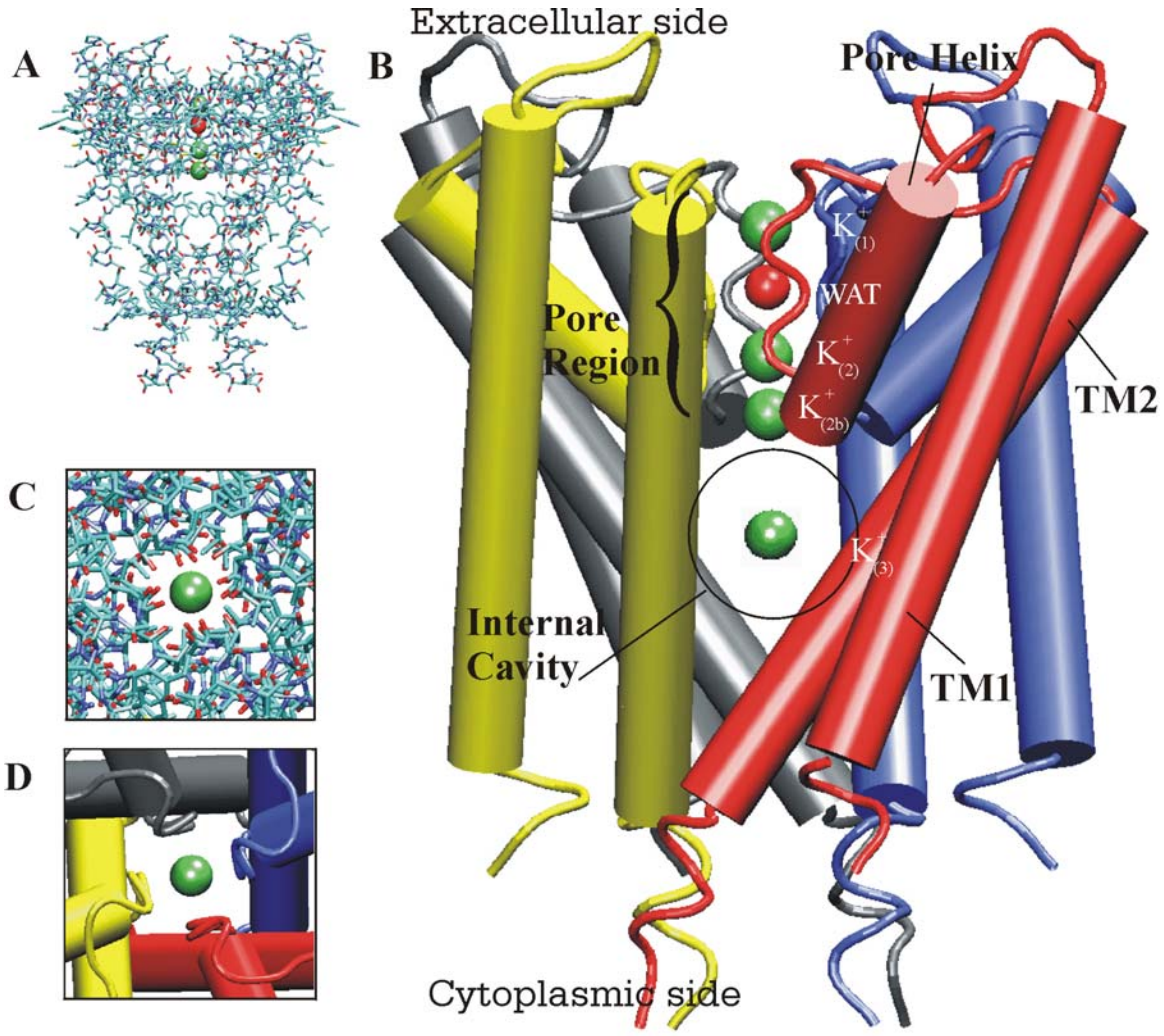

Fig. 1.5. The crystal structure of KcsA channel from *Streptomyces lividans* [8]. The full structure is drawn in stick (A) and in schematic representations (B). In panel (B) the position of the cavity ion $K^+_{(3)}$ is also displayed [44]. (C-D) Top view magnification of the selectivity filter region. Further details are discussed in the text.

(namely Trp-26 and Trp-113 in the cytoplasmic side, Trp-67 and Trp-87 in the extracellular side), as often happens in integral membrane proteins.

The tetrameric structure of the protein is emphasized in Fig. 1.5B by using different colors for the four subunits. Each monomer contains three α helices, represented by cylinders: two transmembrane helices crossing the cell membrane and one shorter helix, located at the extracellular side. The membrane-spanning overall structure is composed of a TM helix bundle forming a sort of funnel with its point of convergence near the

intracellular solution (Fig. 1.5B). The outer helix TM1 is the analogue of S5 in voltage-gated channels (see Fig. 1.3), and forms the majority of the protein-membrane interface. The inner helix TM2, analogue of voltage-gated S6, lines the central pore forming a hydrophobic cavity of ~ 8 Å diameter in the middle of the membrane region. The four shorter helices (the pore helices) lie near the selectivity filter, pointing their axes towards the cavity center.

The selectivity filter region is a narrow tunnel with a diameter of ~ 3 Å, lined with backbone carbonyl oxygens [45]. Protein oxygens replace the K^+ hydration shell in the bulk water, compensating for the loss in energy due to the ion dehydration.

Three binding sites for the potassium atoms were identified by Rb^+ and Cs^+ difference Fourier maps [8,44], in agreement with the traditional view that K^+ channels are multi-ion channels [5,32,33] (green spheres in Fig. 1.5). Backbone carbonylic oxygens belonging to all the four chains bind the potassium ions inside the selectivity filter (Fig. 1.5C-D). An ordered water molecule has also been detected between the two more external (i.e. extracellular) potassium ions (red sphere in Fig. 1.5). An additional K^+ ion is believed to be accommodated in the cavity center, as a diffuse electron density cloud revealed in the difference Fourier maps [8,44]. Because of the closeness between the two more intracellular binding sites detected in crystals ($K^+_{(2a)}$, $K^+_{(2b)}$), it is unlikely that they are simultaneously occupied by two ions [8]. Crystallographers [8,44] therefore proposed that the structure accommodate three ions: two into the selectivity filter binding sites ($K^+_{(1)}$, $K^+_{(2)}$) and one into the internal cavity ($K^+_{(3)}$).

Crystals were grown in neutral conditions (pH = 7.5) in a buffer containing 150mM KCl (or analogous concentrations of CsCl, RbCl, for binding site localization). The Debye-Waller factors of the crystal structure at 3.2 Å resolution are large (backbone average 90 ± 38 $Å^2$).

The barium site, responsible for blocking [1], has also been identified by difference Fourier maps of crystals soaked in 100mM $CaCl_2$ and $BaCl_2$ solutions, respectively [46]. Barium turns out to be localized around the more intracellular potassium binding site $K^+_{(2b)}$.

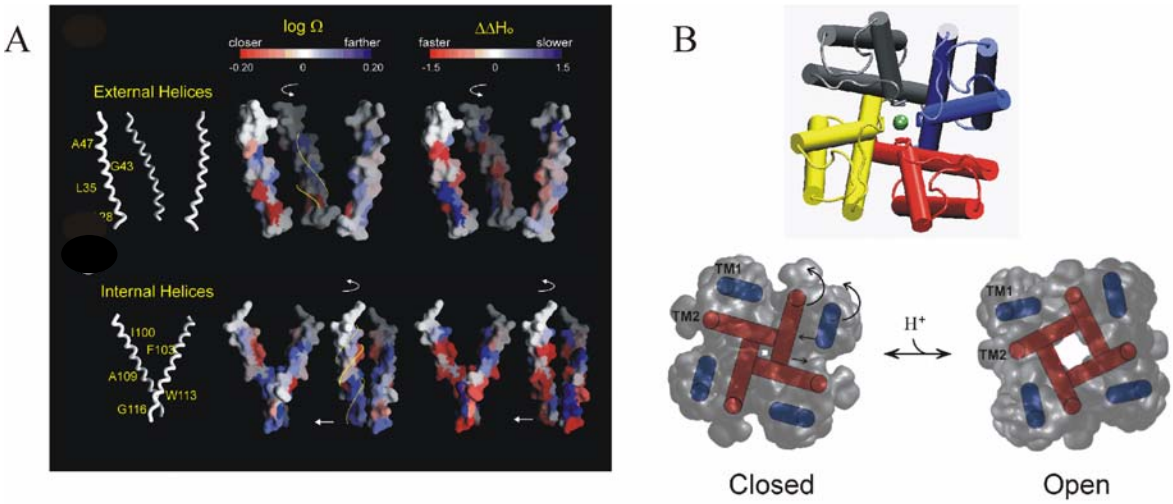

Fig. 1.6 Gating mechanisms of KcsA channel revealed from EPR spectroscopy [9]. (A) Site directed spin labeling of single amino acid in the transmembrane helices at low and neutral pH provides structural information during activation gating. A comparison of EPR data in open and closed conformations gives quantitative measurements of the changes in distances between amino acids in the four subunits and of the spin probe mobility. The overall analysis suggests that the conformational changes illustrated by the white arrows are responsible for the opening of the channel pore. Figure adapted from ref. [9]. (B) Extracellular view of KcsA channel in the closed and open conformations. Upper panel: channel view using the same representation of Fig. 1.5B,D. Lower panel: TM1 and TM2 movements underlying activation gating (figure adopted from ref. [9]).

1.4.3 EPR Spectroscopy data

Electronic Paramagnetic Resonance (EPR) spectroscopy is based on the paramagnetic relaxation of unpaired electrons [47]. In particular, spin labeling of single amino acids with EPR sensitive probes [48] had been used to analyze the structural aspects of KcsA transmembranic helices in different conditions [9,10,40].

Measurements of the probe mobility and of distances between different probes were performed at different pHs. Comparison among the data obtained made it possible to deciphering the gating mechanism at the structural level [9]. As pH decreases, movements of TM1 and TM2 increased the diameter of the intracellular part of the channel pore, opening the channel (Fig. 1.6). The conformational changes mainly involved the channel region that is close to the intracellular point of convergence of the four subunits (see Fig. 1.5). In contrast, the extracellular part of the channel and, in

particular the selectivity filter, remained almost unaffected by the activation movement [9]. The opening of the channel links the internal cavity observed in the crystal structure to the intracellular solution through an aqueous pore.

In conclusion, the EPR data suggested that gating does not affect the selectivity filter region, involving mainly a large rearrangement of TM1 and TM2 helices.

Another recent EPR study has focused on structural aspect of the transmembrane helix TM2 by investigating the polarity of the environment around the EPR probes. The inside surface of TM2 turned out to be surrounded by a polar environment, strongly suggesting the presence of water molecules inside the hydrophobic residues lining the pore [10].

1.5 Open issues and theoretical standpoint

In this section we consider open issues concerning the function of the K^+ channels. Before the availability of the KcsA crystal structure, theoretical approaches to K^+ channel permeation were limited to simplified models, based on a continuum description of the ionic fluxes or on rate-theory [1]. These models, applied to the voltage gated channels fitted experimental data and explain phenomena as current saturation. Some structural theoretical models [49,50] were obtained on the basis of the available structural information derived from experiments (such as circular dychroism, mutational analysis, cysteine scanning mutagenesis, TEA and CTX binding studies, etc). Overall, these models were a valuable help to experimental biophysicists as they were able to rationalize a large amount of data. At the same time, ion channels were investigated at molecular level in model systems. One of the most studied models was gramicidin A, a small peptide formed by alternated L and D amino acids [1]. It has the ability to produce helical pores through lipid membranes, providing an efficient pathway for the passage of monovalent cations. Although gramicidin can adopt many different conformations, depending on the solvent or crystal environment [51],[52-54] most workers in the gramicidin field think [55] that the structure of the channel form when in a bilayer is that determined by Ketchem *et al.* [53]. Gramicidin A has a larger pore than KcsA (see Fig. 1.7), and does not present strong selectivity between K^+ and

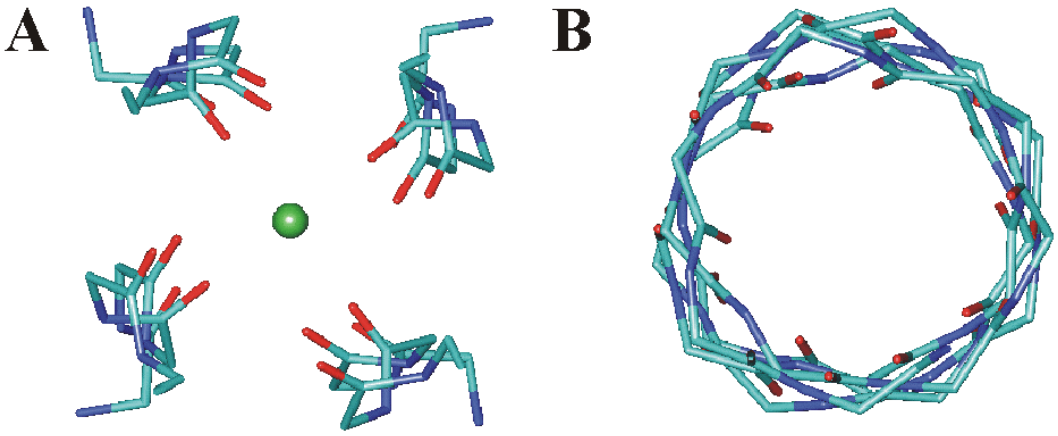

Fig. 1.7 Backbone representation of the pore view of KcsA channel (A) and gramicidin A channel (B). In KcsA only the selectivity filter is shown (from Thr75 to Gly79). K^+ (A) binding sites are also shown as green spheres. Gramicidin model from PDB accession number 1MAG [53,54].

Na^+. Because of its simplicity, it became a paradigm for theory of ion conduction through biological membranes (see next paragraph).

As already mentioned the KcsA crystal structure provided the first solid molecular basis for modeling the complexity of the molecular mechanisms. The use of simulation techniques (i.e. molecular dynamics) might answer fundamental questions on the elementary mechanisms as well as structure-function relationships, hydration properties, long range interactions, and dynamical correlations.

We divided the subject in three parts: permeation mechanism, selectivity, and internal water. This separation is obviously not rigid, because different mechanisms and elements of the channel structure are not independent, interacting to each other. Each paragraph describes the general problem and the state-of-the-art of the theoretical approaches addressed the most important issues. Afterwards, the most relevant topics are discussed in light of the KcsA structure. In the first part we treat the mechanism underlying ion permeation through the selectivity filter, describing the physical factors that are relevant in studying the transport. We also review theoretical approaches based on continuum electrostatics calculations and MD simulations performed on model channels. In the second part, we report the current view of ionic selectivity and the

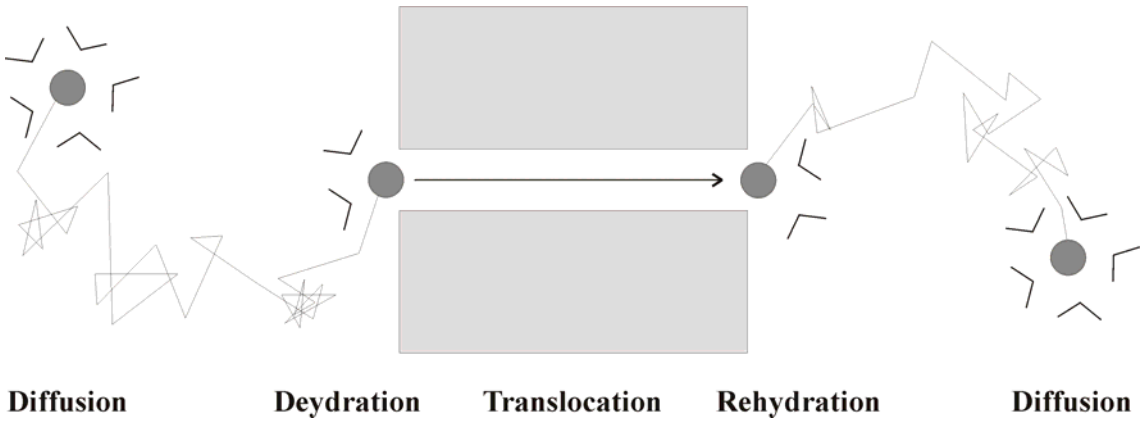

Fig. 1.8 Permeation steps during ion flow through a narrow ionic channel.

theoretical models that has been proposed to explain this phenomenon. Finally, in the third part, we discuss the role of the water into the K^+ channel and, in a more general context, the water behavior in channel pores.

1.5.1 Permeation mechanism

As already mentioned ion rate through ionic channels is extremely fast (10^8 ions/s), and it is close to limits imposed by free ion diffusion in the bulk solution [1]. The understanding of the energies playing a role in ion transport is a fundamental question. In particular the localization along the permeation pathway of the energetic barriers is crucial to understand the rate-limiting step of the process.

The permeation of a single ion trough an ion channel can be divided in five distinct steps: diffusion and binding, dehydration, translocation along the binding sites, rehydration, and diffusion towards the other side of the membrane (Fig. 1.8). Which one of these steps is the limiting factor is still object of discussion.

Before addressing theoretical approaches we review two ingredients which are outmost important for permeation.

Hydration shell properties. Cations in aqueous solution are fully solvated: they have a defined shell of water molecules pointing the negative side of their dipoles towards them in an energetically favorable way. The number of first-shell water molecules, which may be defined by the integral of the radial distribution functions up to its first minimum, depends both on the valence and on the size of the ions. Different MD

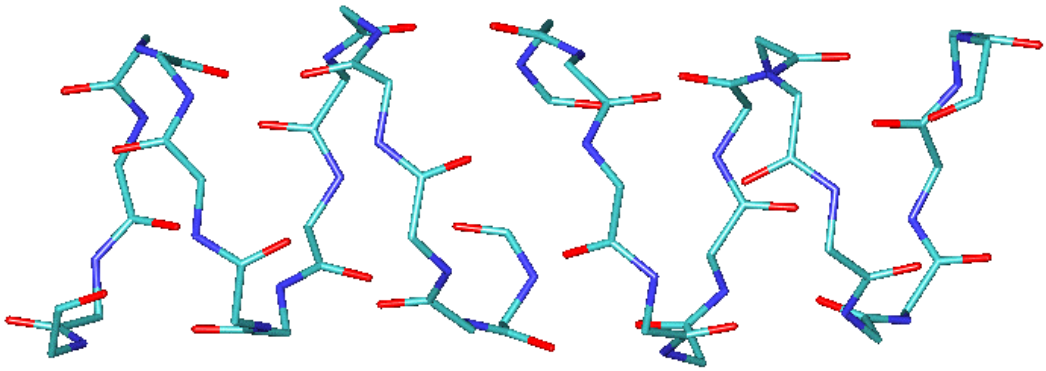

Fig. 1.9 Single file behavior in gramicidin channel. Only backbone atoms of the two subunits are represented. The single-file tunnel for the ions and water molecules is formed by the joining of two gramicidin subunits PDB accession number 1MAG [53].

calculations reported values ranging from 6.3 to 7.8 for K^+, and close to 6 for Na^+ [56]. The water/cation interaction is a dynamical process. The oxygen residence time of Na^+ and K^+ has been estimated to be less than 10^{-10} s [56]. Because the channel pore is a narrow funnel, total or partial dehydration is required for the permeating ions. The dehydration process requires a large amount of energy (the dehydration free energy) that can be provided by the ion interaction with charged or polar protein groups.

Single file behavior. The fact that channel may simultaneously accommodate more than one ion inside the pore have developed the idea that the ions could flow as a single file [5]. In a narrow tunnel, the movements of one ion cannot be independent on that of the other ions, since particles are too large to pass each other inside the pore. Because the presence of water in the channel, ions flow and water movements needs to be cross-coupled.

Continuum models. In this approaches a simplified scheme mimics the ion flow. Ions are represented as charged spheres immersed in a high dielectric medium (water) passing through pores in a slab of low dielectric medium (the channels and the membrane) [57]. As an ion approaches the pore induces polarization charges at dielectric phase boundaries, changing the total energy of the system. Free energy profiles may be calculated along the pore axis in this approximation and the channel conductance may therefore be evaluated. In these continuum models the internal

barriers are usually exaggerated compared to those experimentally observed in gramicidin [57].

Molecular models. The most studied ion channel model is gramicidin A. The peptide channel represents a clear example of single-file behavior, as X-ray structure had directly revealed [52]. In this narrow pore, cations move by exchanging water and protein ligands. Free energy perturbation studies [7] revealed that small translocation energy is required for an ion movement inside the peptide channel, suggesting that the rate limiting step for ion transport are the barriers at the exit and at the entrance of the helix. The CO groups in the vicinity of the ion are significantly deflected, lowering the barriers encountered by ionic movements, thereby improving the rate of the ligand exchange. The hydration-rehydration reactions are tough to be a limiting factor also for highly selective channel, like potassium channels [1].

Comparison with KcsA. In the KcsA structure, the presence of the cavity significantly reduces the length of the dehydrated path of a permeating ion from the ~ 34 Å membrane thickness to the ~ 12 Å selectivity filter length. The K^+-protein interactions are therefore shortened in space and (in the extracellular side) limited to the selectivity filter. The binding sites detected by the X-ray shows that the carbonyl oxigens of the protein replace the coordination shell of the alkali ions when not fully hydrated. The crystal structure also confirmed the multi-occupancy nature of the narrow KcsA channel pore. The narrowness of the pore suggests that single-file behavior of the ions should also involve the water molecules presents into the selectivity filter.

From the above discussion it is confirmed that two basics factors seems to be relevant for a better comprehension of the potassium channel permeation mechanisms: the dehydration process and the single file behavior.

1.5.2 Selectivity

The high specificity in cation selectivity of potassium channels is surprising if compared to their fast flux rate. Eisenman provided [58,59] a first attempt to explain the mechanisms of ionic selectivity for cations. His simple theory was based on the difference between cation hydration energy and favorable interaction with charged or

polar group in the binding site within the channel. The hydration free energy G_{hydr} of an ion of charge q and radius r was modeled using the Born approximation [60]:

$$G_{hydr} = \frac{q^2}{8\pi\varepsilon_0\varepsilon_w r},$$

where ε_w is the dielectric constant of water. The interaction free energy G_{int} with a ligand of charge q_l and radius r_l was written in the same continuum approximation scheme as:

$$G_{\text{int}} = \frac{qq_l}{8\pi\varepsilon_0\varepsilon_w(r+r_s)}.$$

From the differences between G_{hydr} and G_{int} Eisenman obtained, as a function of r_s, the 11 sequences in cation selectivity that have been found in cell membranes [58,59].

Site directed mutagenesis experiments revealed that the selectivity properties of both potassium [27,29] and sodium [61-63] channels could be changed by mutating a single amino acid. Anyway, it has not been possible so far exchanging K^+ for Na^+ selectivity by mutating charge or polar groups.

Several discussions can be found in the literature on the role of geometrical factors in ionic selectivity [1,45]. Channel pores are assumed to be rigid molecular sieves, able to efficiently distinguish ions basing on the size of their radius with or without hydration water molecules [1]. Mechanisms of selectivity were proposed for a variety of cation channels (i.e. K^+, Na^+, Ca^{2+}, and endplate channels) geometrically comparing cations with a putative shape of the selectivity filter [1].

A prove that the ionic selectivity can arise from the geometrical properties of the inner core alone has been recently reported [64]. The microscopic model is based on experimental physical-chemical properties of ions in solution and takes into account the ion hydration free energy loss into the pore. Using expression for the permeability ratio based on Langevin and Fokker-Planck equations, selectivity sequences for all kinds of channels were fairly reproduced also in the absence of any ionic interactions with charged or polar groups. The theoretical permeability ratio of two ionic species A, B can be expressed by:

$$\frac{P_B}{P_A} = \frac{\tau_B}{\tau_A} \exp(-\tfrac{1}{RT}(G_B^{(s)} - G_A^{(s)})) ,$$

where $G_{A,B}^{(s)}$ are the Gibbs free energies of the two ionic species calculated at the selectivity filter, and $\tau_{A,B}$ are prefactors depending on friction, ionic masses and the free energy profile. Evaluation of this expression in different conditions led to the conclusion that the dominant contribution comes from the exponential term, and therefore the permeability ratio is almost independent on the extent of the binding energies. In conclusion, ionic selectivity may be explained also without supposing interactions with charged or polar protein groups.

Molecular Dynamics simulations performed on gramicidin A models helped understand the mechanism of valence selectivity [7,65-68]. The CO groups of the gramicidin backbone support a more favorable interaction with K^+ ions than that supported by NH groups with Cl^- ions [65]. Anions are therefore almost rejected from the pore. Proton transfer in ion channel requires a special treatment, because special mechanisms are implied in the H^+ translocation, as suggested by *ab initio* MD [69].

In conclusion, the origin of selectivity in K^+ channels is still a debated open issue. The mayor role on the basic mechanism for ionic selectivity might be due to a simply steric effect, that involves the ion and one or more water molecules, or could be merely due to energetic differences in the interaction with binding groups.

1.5.3 The water inside the channel

Ion channels have water inside their internal pore. In the interior of KcsA channel two distinct regions are supposed to be occupied by water molecules during the transport process: the selectivity filter and the internal cavity (see Fig. 1.5).

In the selectivity filter, although only one water molecule had been detected in the crystal, is reasonably assumed that, because the single file behavior, in intermediate permeation states also the other K^+ binding sites could be water filled. The internal cavity of the channel significantly reduces the region inside the channels where ions need dehydration (Fig. 1.5). This cavity is surrounded by hydrophobic residues [8], is water filled [8,10], and is able to contain a monovalent cation [8,44]. The hydrophobic

character of the residue lining the internal cavity can be functionally linked to the high throughput of K^+ channels [8]. The loss of polar residues in this region of the channel limits the strong protein-ion interactions to the selectivity filter region, providing a relatively inert surface to a permeating ion. The presence of water was postulated by crystallographers [8] and directly proved by EPR studies [10]. Different water content has been proposed for the cavity: 50 water molecules [44], 38 [70], 30 [71], and15-18 [72].

The properties of water when confined in small spatial region are different to those of the bulk solution, like happens for liquids in general [73]. Differences comes most of all in the dynamical properties, like changes in the dielectric constant, prolonged correlation times and collective motions. Although for a detailed description of the water dynamics an *ab initio* dynamical approach might be required [74,75], many properties can be qualitatively described by using classical effective potentials.

Studies of simplified model systems of channels evidenced the anomalous behavior of the confined water in pores [57,76-79]. In gramicidin-like pores 6-8 water molecules are placed in the pore as a single file (Fig. 1.9). In the narrow tunnel the presence of ions dramatically affects the dielectric properties of the water chain, lowering the orientational mobility of the molecules [76].

More detailed atomic models of transmembrane pores formed by α-helix bundles has been performed *in vacuo* [11,80,81], in water-octane-water phases used as membrane-mimetic environment [82-86], and in phospholipid bilayers [87,88].

In synthetic leucine-serine ion channels [82,88], trajectory analysis has revealed that the dipole moment of the pore water molecules is aligned along the axis of the pore by the surrounding helix dipoles. This results has been obtained immersing the helix bundle in an octane slab [82], or in phospholipid bilayer [88], indicating that water properties are relatively unperturbed by the membrane model used. Similar behavior has been observed for the alamethicin channel in vacuo [11] and in lipid bilayer [87].

The reduced mobility of the polarized molecules within pores has the effect to lower the water dielectric constant [11]. These changes could in principle affect not only the water-protein interactions, but also the long-range water-mediated electrostatic

interactions between ions into the pore. This peculiar behavior might play some role in the KcsA channel conduction.

The above discussion shows that, in narrow channels, the modeling of the aqueous pore as a continuum medium with space-independent dielectric constant may led to underestimate the saturation effect in orientational polarizability of the molecules. The use of dynamical approaches with explicit water might be requested for an accurate description of the protein-water and of the ion-ion interactions in KcsA potassium channel.

1.6 Aim of the present work

In this section we outline the purposes of the present work.

Our molecular models include ions, explicit water and the KcsA structure immersed in a n-octane slab to mimic the hydrophobic membrane environment. As first goal, we will verify whether the overall structure of our model used is able to remain stable during the time scale accessible by current simulations (few ns). This is not trivial, as up to now simulations in water/n-octane phases were performed only in helix bundle models[82-85]. Comparison with the available EPR data will provide further information on the validity of our scheme.

Because of the symmetry of the permeation process (see Fig. 1.8), the first three fundamental steps will be addressed: the ion diffusion and binding, the dehydration, and the ion translocation into the selectivity filter. From the analysis of these steps we will try to answer the question whether the ion dehydration could be a rate-limiting step in ion transport. Comparison between the behavior of different cations might also provide insight on the physical origin of selectivity.

Ion diffusion from bulk water to the channel mouth might be driven by long range electrostatic interactions between the ion and protein groups. Analysis of the dynamics and of the potential electrostatic energy profiles in the channel mouth may provide a qualitative picture of the driving forces in this first step. The dehydration phase might be either the bottleneck of the ionic transport or, on the contrary, a spontaneous process speeded up by the specific engineered protein structure. Differences in the number of

water molecules that could remain in the K^+ or Na^+ hydration shell after binding may give rise of the key role of water in the molecular recognition.

The full solvated atomic model of the channel will allow us to take into account the full complexity of the protein-ions, protein-water, and ion-water interactions. The water properties inside the channel will be explored to address the issue of water polarization in the cavity. We will also investigate whether these water molecules could play any role in ion permeation.

The last purpose is the understanding the K^+ interactions that take part during the translocation through the selectivity filter. The study of the changes in the protein chemical and structural properties during this ion movement may help in understanding the nature and the location of permeation barriers in this region of the channel.

2 Methods

In this chapter we shortly summarizes the theoretical methods that we have used. For general references for the treated arguments see refs. [89-91]. In the next chapter we report the parameters used in the simulations and the procedure followed for building the starting molecular model.

2.1 Classical molecular dynamics simulations

In molecular dynamics a set of configurations is generated integrating the Newton's equation of motion. For a system of N particles of masses $\{m_i\}$ and positions $\{\mathbf{r}_i\}$, we may write the equation of motion as:

$$m_i \ddot{\mathbf{r}}_i = -\nabla_{\mathbf{r}_i} E \qquad i = 1, \mathrm{K}, N$$

The potential energy E acting on the atomic nuclei may be described, neglecting the electronic interactions, by simple functions of the ionic positions themselves $E = E(\{\mathbf{r}_i\})$.

The force-field is obtained by analytical functions that are derived by fitting experimental data. In this section we introduce the force-field parameterization (§ 2.1.1) as well as computational tools used in our simulations (from § 2.1.2 to § 2.1.6). Details about the molecular model and the specific parameters we used in our calculations will be reported in the next chapter.

2.1.1 The force field

Here we summarize the feature of the AMBER force field. For a full and detailed description of the parameter assignment see ref. [92].

The force field is based on the following two-body potential energy function:

$$E = E_{bonds} + E_{angles} + E_{dihedrals} + E_{van\ der\ Waals} + E_{electrostatic} =$$

$$= \sum_{bonds} K_r (r - r_{eq})^2 + \sum_{angles} K_\theta (\theta - \theta_{eq})^2 + \sum_{dihedrals,n} \frac{V_n}{2}[1 + \cos(n\phi - \gamma)] +$$

$$+ \sum_{i<j} \left[\frac{A_{ij}}{(r_i - r_j)^{12}} - \frac{B_{ij}}{(r_i - r_j)^6} + \frac{q_i q_j}{4\pi\varepsilon_0 |r_i - r_j|} \right]$$

$E_{bonds} + E_{angles}$. Bond stretching and angle bending are taken in account by armonic energy terms involving the interested atoms. The equilibrium bond and angle values r_{eq}, θ_{eq}, as well as the spring strengths K_r, K_θ are adjusted to reproduce normal mode frequencies.

$E_{dihedrals}$. The torsion energy is decomposed in its Fourier terms. Dihedral parameters are calibrated on small model compounds, comparing the energies with those obtained by *ab initio* quantum chemical calculations. Improper dihedral angles are inserted between non linked bonds to preserve planarity in aromatic rings.

$E_{van\ der\ Waals}$. A Lennard-Jones potential is used to mimic the van der Waals interations. Parameters are obtained so as to reproduce chemical-physical properties in simple organic liquids (densities, enthalpies of vaporization, free energies of solvation, etc).

$E_{electrostatic}$. The electrostatic energy is evaluated by using the Restrained Electrostatic Potential (RESP) partial charges [93]. These charges have the properties of accurately reproduce the electrostatic potential multipoles outside the molecule, and they were calculated in the following way. *Ab initio* quantum chemical calculations are performed on small molecules and the electrostatic potential $\{V_j\}$ are calculated on M grid points outside the molecule.

The point charges $\{q_i\}$ are fitted minimizing χ^2_{esp}:

$$\chi^2_{esp} = \sum_{j=1}^{M} (V_j - \overline{V}_j)^2 + \sum_{i=1}^{N} \left[(q_i^2 + b^2)^{1/2} - b \right],$$

where $\{\overline{V}_j\}$ is the electrostatic potential generated by the point charges, a and b are appropriate parameters. The first term of χ^2_{esp} fits the potential generated by the *ab initio* one. The hyperbolic terms tends to minimize the absolute charges, avoiding the effect of poorly determined buried atom charges (like happens in ESP charges [94]).

The Electrostatic and van der Waals interaction energies are calculated only between atoms in different molecules or for atoms in the same molecule separated by at least three bonds.

2.1.2 The integration algorithm

Fixed the energy function for the molecular interactions, the trajectory of the system is in principle determined by its initial conditions: atomic positions and velocities. In practice, the Newton's equations of motions cannot be solved analytically. The integration of the equations of motion is achieved using finite difference methods. The time variable is discretized by assuming that no variations of the force acting to the atoms occurs in the time step δt. Various algorithms have been proposed for the numerical integration, differing for accuracy and computational speed [89,90].

We used the velocity Verlet algorithm that gives the positions ***r*** and velocities ***v*** at time $t+\delta t$ using the following formulas [95]:

$$\begin{cases} \mathbf{r}(t+\delta t) = \mathbf{r}(t) + \delta t \mathbf{v}(t) + \frac{1}{2}\delta t^2 \mathbf{a}(t) \\ \mathbf{v}(t+\delta t) = \mathbf{v}(t) + \frac{1}{2}\delta t \left[\mathbf{a}(t) + \mathbf{a}(t+\delta t) \right] \end{cases}$$

where **a** is the acceleration.

This algorithm has also the property to preserve the phase space measure [90].

2.1.3 Constraints

In a MD simulation the highest frequency motions are the bond vibrations. In particular light atoms, like hydrogen, are involved in the fastest bond stretching vibrations. These frequencies are often of little interest in classical simulations of biological systems. The use of constraint allows keeping these bond lengths fixed during the some irrelevant degree of freedom. The time step can be therefore increased without prejudicing the accuracy of the simulation.

The set of N_c molecular constraints σ_k, one for each constrained bond, has the following form:

$$\sigma_k(\mathbf{r}_1,\mathrm{K}\ ,\mathbf{r}_N)=0 \qquad k=1,\mathrm{K}\ ,N_c$$

The satisfying of the N_c constraints can be accomplished by applying the Lagrange's multiplier method. An extra term is added to the potential energy function, and the equation of motions became:

$$m_i\ddot{\mathbf{r}}_i=-\nabla_{\mathbf{r}_i}E-\nabla_{\mathbf{r}_i}\sum_{\mathrm{k}=1}^{\mathrm{N_c}}\lambda_k(t)\sigma_k(\mathbf{r}_1,\mathrm{K}\ ,\mathbf{r}_N) \qquad i=1,\mathrm{K}\ ,N$$

After the time step δt, the system coordinate $\mathbf{r}_i'(t+\delta t)$ will differ by a quantity $\delta\mathbf{r}_i$ with respect to that of the unconstrained system $\mathbf{r}_i(t+\delta t)$: $\mathbf{r}_i'(t+\delta t)=\mathbf{r}_i(t+\delta t)+\delta\mathbf{r}_i$. This correction may be found by using an exact methods that requires the solution of a system of N_c linear equations in $\{\lambda_k\}$[96], but this procedure is usually avoided because it is computationally expensive.

The SHAKE algorithm used in the simulations allows satisfying the set of *k* olonomic constraints by using an iterative procedure [96]. For each atom involved in the constraints, an additional positional shift $\delta\mathbf{r}$ in the bond direction is added into the Verlet algorithms in order to subsequently satisfy all the *k* constraints. The fulfillment of the *k*th constraint partially destroys the previous ones. The procedure is therefore iterated up to the desired convergence.

2.1.4 Temperature control

Temperature has been kept close to the desired target value T_0 using the method illustrated by Berendsen *et al.* [97].

The system is virtually coupled with a thermal bath at temperature T_0. For each atom *i*, a Langevin equation replaces the equations of motion to describe the coupling between the two systems:

$$m_i \mathbf{a}_i = \mathbf{F}_i + m_i \gamma \left(\frac{T_0}{T} - 1 \right) \mathbf{v}_i$$

where T is the instant temperature of the system, and γ is the friction coefficient.

At each time step δt velocities are therefore scaled by a factor $\lambda = 1 + \frac{\delta t}{2\tau}\left(\frac{T_0}{T} - 1 \right)$, where $\tau = (2\gamma)^{-1}$.

2.1.5 Electrostatics evaluation

In molecular dynamics, periodic boundary conditions are often used to minimize boundary effects. In this scheme, a particle interacts with all other *N-1* particles into the box and with all their images in an infinite array of periodic cells [89]. The electrostatic potential energy *V* of the infinite system can be written as:

$$V = \frac{1}{4\pi\varepsilon_0} \frac{1}{2} \sum_{|\mathbf{n}|=0}^{\infty} \sum_{\substack{i=1 \\ (i \neq j \text{ if } \mathbf{n}=0)}}^{N} \sum_{j=1}^{N} \frac{q_i q_j}{|\mathbf{r}_{ij} + \mathbf{n}|},$$

where **n** are the direct lattice vectors.

The infinite series converges extremely slowly and calculating *V* from this expression is highly inefficient. To overcome this problem Ewald introduced a trick for dividing the summations in two sums which converges much more rapidly. At each charge position r_i, a gaussian charge distribution of opposite total charge – q_i, is added (ρ_i^s) and subtracted (ρ_i^G), so that the total point charge distribution of the system $\rho(r)$ may be written as:

$$\rho(r) = \rho(r) + \rho^s(r) - \rho^G(r) =$$
$$= \sum_{i=1}^{N} q_i \delta(r - r_i) + \sum_{i=1}^{N} q_i (\alpha/\sqrt{\pi})^3 e^{-\alpha^2 (r - r_i)} - \sum_{i=1}^{N} q_i (\alpha/\sqrt{\pi})^3 e^{-\alpha^2 (r - r_i)}$$

Let us consider the $\rho(r)+ \rho^s(r)$ term of the electrostatic potential V^s, and the - $\rho^G(r)$ term V^G.

For the first term we obtain:

$$V^s = \frac{1}{4\pi\varepsilon_0} \frac{1}{2} \sum_{|\mathbf{n}|=0}^{\infty} \sum_{\substack{i=1 \\ (i \neq j \text{ if } \mathbf{n}=0)}}^{N} \sum_{j=1}^{N} \frac{q_i q_j \operatorname{erfc}(\alpha |\mathbf{r}_{ij} + \mathbf{n}|)}{|\mathbf{r}_{ij} + \mathbf{n}|},$$

where erfc is the complementary error function $\operatorname{erfc}(x) = \frac{2}{\pi} \int_x^{\infty} e^{-t^2} dt$.

Calculation of V^s in real space is now easier, because the opposite charged $\rho^s(r)$ distribution shields the point charges, yielding negligible the electrostatic contribution when $|\boldsymbol{r}_{ij} + \mathbf{n}|$ is large. The computational effort of the V^s sums may be further reduced by choosing the α parameter as large as the sum is effectively zero when r_i and r_j are beyond a certain cutoff (i.e. 10 Å). In this way it becomes O(N).

The second term V^G can be faster evaluated in the reciprocal space:

$$V^G = \frac{1}{4\pi\varepsilon_0} \frac{1}{2\pi L^3} \sum_{k \neq 0}^{\infty} \sum_{i=1}^{N} \sum_{j=1}^{N} q_i q_j \frac{4\pi^2}{k^2} e^{-k^2/4\alpha^2} \cos(\mathbf{k} \cdot \mathbf{r}_{ij})$$

The convergence is much more rapid that the original point charge sum. This expression may be calculated with an O(N^2) operations. To further improve the efficiency approximate ways to perform this sum [98,99] were proposed. An efficient Particle mesh Ewald implementation consists in interpolating the reciprocal space potential on a grid using smooth function [98,99]. Therefore, the sum can be evaluated by using order $N \cdot \ln(N)$ fast Fourier transform algorithms.

2.1.6 Calculated properties

Root mean square displacement. The root mean square displacements (rmsd's) of a set of snapshots $\{\mathbf{r}_i\}$ with respect a referring structure $\mathbf{r}^*$ is calculated using [100]:

$$rmsd = \sqrt{\frac{1}{N}\sum_{i=1}^{N}(\mathbf{r}^* - \mathbf{r}_i)^2}$$

Radial distribution functions. Radial distribution functions *g(r)* between two species A and B is calculated by:

$$g(r) = \frac{N(r)\cdot V}{4\pi r^2 dr}$$

where

$$N(r) = \left\langle \frac{1}{N_A N_B - N_{AB}} \sum_{\substack{i=1 \\ (i\neq j)}}^{N_A} \sum_{j=1}^{N_B} \delta(r - |\mathbf{r}_{Ai} - \mathbf{r}_{Bj}|) \right\rangle .$$

$N_{A(B)}$ is the number of atoms of species A(B), N_{AB} is the number of atoms common to both species, $\mathbf{r}_{Ai(Bj)}$ are the atoms coordinates, and *V* is the volume.

2.2 Electrostatics calculations

Electrostatic interactions play an important role in biological structures [101]. The availability of atomic scale structure of protein and nucleic acids has allowed understanding the electrostatic contribution of specific molecular interactions. A quantitative description of these interactions assumes also a practical importance in applied biological science (e.g. drug design).

Although an explicit treatment of the single water molecules is crucial in many cases, a continuum approximation of the solvent medium may provide a qualitative description of electrostatics with a small computational effort.

In the continuum approximation the electrostatic potential $\phi(r)$ is determined by the Poisson-Boltzmann (PB) equation [101]. Using dimensionless units kT/q:

$$\nabla \cdot [\varepsilon(r)\nabla\phi(r)] - \varepsilon(r)\kappa(r)^2 sinh[\phi(r)] + 4\pi\rho^f(r)/kT = 0$$

$\rho^f(r)$ is the fix charge density of the molecule; $\varepsilon(r)$ is the (space-dependent) dielectric constant; $\kappa(r) = 1/\lambda^2$ depends on the Debye lenght $\lambda = \sqrt{ekT/8\pi q^2 I}$ of the solvent, where I is the ionic strength of the bulk solution.

A numerical solution of the PB equation may be obtained using finite difference methods on a grid [102]. As a first step the molecular surface is generated using a spherical probe of 1.4 Å (the water Van der Waals radius). A grid is therefore generated (typical mesh ~ 1 Å) and a charge is assigned to each point mesh if it is within an atom sphere. According to the surface, a high dielectric constant value is then assigned to the grid points that lies in the external part of the macromolecule, which are supposed belonging to the solvent (ε = 80), and a low dielectric constant value is assigned to the remaining grid points. The meaning of the latter is to mimic the thermal charge shielded of the protein, and usually is chosen in the range ε = 2, ε = 8. Further tricks and smoothing algorithms are used in order to obtain the good results using a large spaced grid [102,103].

2.3 Electronic structure calculations

A rigorous treatment of the properties of the ground state $|\Psi\rangle$ a molecule is described by the Scrödinger equation for the interacting ions and electrons.

$$H|\Psi\rangle = E|\Psi\rangle$$

The Hamiltonian H of a system with N electrons can be written (in atomic units):

$$H = T + V_{ee} + V_{ext} = -\frac{1}{2}\sum_{i=1}^{N}\nabla_i^2 + \frac{1}{2}\sum_{i\neq j}^{N}\frac{1}{|\mathbf{r}_i - \mathbf{r}_j|} + \sum_{i=1}^{N}V_{ext}(\mathbf{r}_i),$$

where V_{ext} is the external potential applied to electrons, including the ion-electron electrostatic terms.

Some approximations are required to make the problem feasible in practice. In this section we reviews the basic concepts of the methods (§ 2.3.1) and the approximations and implementation used (§ 2.3.2, § 2.3.3). Because in the present work we are interested only close-shell systems we limit the treatment to this special case.

2.3.1 Density Functional Theory and Kohn-Sham formulation

An useful framework to solve the quantum problem is given by the Density Functional Theory (DFT). This theory allows to replace the Scrödinger equation for the *N*-electron wave function with simpler calculational schemes involving the electron density $\rho(r)$. This drastic reduction is due to two theorems by Honemberg and Kohn. They were able to write a variational principle for an energy functional of the density alone.

The Hohenberg and Kohn theorems state as follows [104]:

The external potential V_{ext} is determined, within a trivial additive constant, by the electron density $\rho(r)$. Therefore, all the properties of the system can by derived by the knowledge of the density $\rho(\mathbf{r})$ alone. In particular, the total energy $E = <\psi | H | \psi>$ may be written as a functional of $\rho(\mathbf{r})$:

$$E[\rho] = T[\rho] + V_{ee}[\rho] + V_{ext}[\rho] = T[\rho] + V_{ee}[\rho] + \int d\mathbf{r} v_{ext}(\mathbf{r})\rho(\mathbf{r})$$

Note that the first two terms $E_{HK}[\rho] = T[\rho] + V_{ee}[\rho]$ of the above equation are completely independent on the external potential. E_{HK} is the so-called Hohenberg-Kohn (HK) functional and finding better approximations to it are the main finding of DFT theory.

The ground state energy E_0 of the system is the minimum of the total energy functional $E[\rho]$ with respect variations of ρ preserving $\int d\mathbf{r}\rho(\mathbf{r}) = N$. This theorem is analogous to the variational principle for wave functions.

This variational principle requires that the ground state density satisfy the following stationary principle

$$\frac{\delta}{\delta n}\left[E[\rho]-\mu\int d\mathbf{r}\rho(\mathbf{r})\right]=0\,, \qquad (1)$$

where μ is the Lagrange multiplier introduced to impose the normalization condition.

To solve equation (1) Kohn and Sham (KS) intoduced [105] a solution scheme based on an ortonormal set of *N* independent single particle wave functions, the KS orbitals ψ_i. The basic idea is to choose a basis where the kinetic term of the HK functional may be written in a simple way in terms of these orbitals, and handling separated the residual corrections. They associated to (1) a corresponding non-interacting reference system with the following hamiltonian [105]:

$$\hat{H}_s=\sum_{i=1}^{N}(-\tfrac{1}{2}\nabla_i^2)+\sum_{i=1}^{N}v_{eff}(\mathbf{r}_i)$$

where the *N* occupied orbitals are the lowest eigenstates of the one-electron hamiltonian:

$$[-\tfrac{1}{2}\nabla_i^2+v_{eff}(\mathbf{r})]\psi_i=\varepsilon_i\psi_i\,, \qquad (2)$$

and v_{eff} is a an opportune one-body effective potential. Kohn and Sham provided a procedure for the calculation of v_{eff}, as shown further. In this system simple formulas for $\rho(r)$ and for $T[\rho]$ may be written:

$$\rho(\mathbf{r})=\sum_{i=1}^{N}|\psi_i(\mathbf{r})|^2$$

$$T_s[\rho]=\sum_{i=1}^{N}<\psi_i\,|-\tfrac{1}{2}\nabla^2\,|\psi_i>$$

The HK functional may be rewritten as a function of T_S:

$$E_{HK}[\rho] = T_s[\rho] + \frac{1}{2}\int d\mathbf{r}d\mathbf{r}' \frac{\rho(\mathbf{r})\rho(\mathbf{r}')}{|\mathbf{r}-\mathbf{r}'|} + E_{xc}[\rho]$$

Note that the first term T_S (the kinetic energy of a *non-interacting* system, i.e. without V_{ee}) differs with respect T. The second term is the "classical" part of the electron interaction energy V_{ee}. The third term E_{xc} is the exchange correlation energy. It includes the difference between T and T_S, and the non-classical part of V_{ee} (i.e. the exchange energy).

The Euler-Lagrange equations (1) becomes:

$$\begin{cases} \mu = \dfrac{\delta E_{HK}[\rho]}{\delta\rho(\mathbf{r})} = v_{eff}(\mathbf{r}) + \dfrac{\delta T_s[\rho]}{\delta\rho(\mathbf{r})} \\ v_{eff}(\mathbf{r}) = v_{ext}(\mathbf{r}) + \int d\mathbf{r}' \dfrac{\rho(\mathbf{r})}{|\mathbf{r}-\mathbf{r}'|} + v_{xc}(\mathbf{r}) \end{cases} \quad (3)$$

A density satisfying the above equation may be obtained by solving the set of N one-electron equations (2).

Equations (2) and (3) may be solved in a self-consistent way: for a given set of starting orbitals ψ_i, we evaluate v_{eff} using eq. (3), and solve eq. (2) to determine a new set of orbitals. The cycle is repeated unless convergence in the KS orbitals (and therefore in density) is achieved.

2.3.2 Local Density Approximation

In the description of the KS equations in the previous paragraph, we did not specify the form of the exchange correlation functional $E_{xc} = \int d\mathbf{r} v_{xc}(\mathbf{r})$. Many efforts have been made for finding an accurate expression for this functional.

Kohn and Sham [105] proposed the Local Density Approximation E_{xc}^{LDA} for the exchange correlation energy. The exchange-correlation functional is calculated as in each point $\mathbf{r}$ it had the same value that the exchange-correlation energy of a homogeneous electron gas:

$$E_{xc}^{LDA}[\rho] = \int d\mathbf{r}\rho(\mathbf{r})\varepsilon_{xc}^{hom}[\rho(\mathbf{r})]$$

The exchange-correlation energies per particle of a uniform interacting electron gas at different densities $\varepsilon_c^{hom}[\rho]$, define completely the LDA functional. The exchange energy component of $\varepsilon_x^{hom}[\rho]$ can be exactly calculated for an homogeneous electron gas [91]:

$$\varepsilon_x^{hom}[\rho] = -\tfrac{3}{4}\left(\tfrac{3}{\pi}\right)^{1/3}\rho^{1/3}$$

Accurate calculation of the correlation energies at several densities may be obtained using Quantum Monte Carlo technique [106]. This crude approximation, although exact only in the limit of uniform densities, has been revealed to be a good starting point for the determination of many ground state properties of atoms and molecules, despite these systems are much distant to be homogeneous.

The LDA approximation encounters difficulties in describing H-bond systems and therefore is not optimal for biomolecules. To improve E_{xc} one can include corrections depending on the gradient of the density. In our calculations we used the gradient corrections approximations (GCA) of Becke [107]:

$$E_x^B = E_x^{LDA} - \beta\int \rho^{4/3}\frac{x^2}{(1+6\beta\sinh^{-1}x)}d\mathbf{r}, \qquad \text{with}: x = \frac{|\nabla\rho|}{\rho^{4/3}}$$

The β parameter was obtained by fitting E_x values obtained byatomic Hartree-Fock calculations for noble gas atoms [107].

For the correlation energy we have used the parameterization introduced by Lee, Yang and Parr (LYP) [108,109]:

$$E_c = -a\int \frac{1}{1+d\rho^{-1/3}}\left\{\rho + b\rho^{-2/3}\left[C_F\rho^{5/3} - 2t_W + (\tfrac{1}{9}t_W + \tfrac{1}{18}\nabla^2\rho)\right]e^{-c\rho^{-1/3})}\right\}d\mathbf{r}$$

where $C_F = \tfrac{3}{10}(3\pi^2)^{2/3}$, and $t_W(\mathbf{r}) = \tfrac{1}{8}\frac{|\nabla\rho(\mathbf{r})|^2}{\rho(\mathbf{r})} - \tfrac{1}{8}\nabla^2\rho$

and $a = 0.049$, $b = 0.132$, $c = 0.2533$, $d = 0.349$.

2.3.3 Plane wave and pseudopotentials

To solve the Kohn-Sham equations, is necessary to write the KS in a finite basis set. In simulating solids periodic boundary conditions are applied to an elementary cell. We have used a plane wave basis set. For each Bloch function $\psi_i^{\mathbf{k}}$ of band i and momentum **k**, we can write:

$$\psi_i^{\mathbf{k}}(\mathbf{r}) = \sum_G c_i^{\mathbf{k}+\mathbf{G}} e^{i(\mathbf{k}+\mathbf{G})\cdot\mathbf{r}} ,$$

where **k** belongs to the first Brillouin zone of the crystal, and **G** is a reciprocal lattice vector.

Because the non-local nature of the plane waves, usually a larger amount of basis function is necessary with respect to other more localized basis set. The use of plane waves has the advantage that the basis set does not depend on the atom geometry in the cell. This choice is made efficient by using fast Fourier transform algorithms.

In simulating molecular cluster a common procedure is to choose a large cell (a supercell) around the simulated molecules, in order to reduce the interactions between the system and its images. In our calculation we used a procedure that allows treating the system as isolated [110].

The dimension of the basis set is determined by the choice of a maximum cutoff E_{cut} for the kinetic energy T^{PW} of the plane waves by the condition:

$$T^{PW} = \frac{1}{2} |\mathbf{k} + \mathbf{G}|^2 \leq E_{cut}$$

Use of the plane waves is not indicated to reproduce the rapid oscillations of the wave function in closeness of the atomic nuclei. In particular the core electrons, which are highly localized around the nuclei, need a very large set of plane waves for an accurate description. However, the core levels are well separated in energy from the valence electrons, and they do not play a role in the chemical bonding properties of the system.

Thus, the core electron orbitals can be omitted from the KS equations and their effect on the valence electrons is described by using effective potentials (the pseudopotentials). Pseudopotentials are usually derived from all electron (AE) atomic

calculations, comparing the AE wave function with the pseudo wave function obtained by omitting the core electrons and including the pseudopotential term. We summarize below the common features that any norm-conserving pseudopotentials needs to satisfy:

(i) The valence AE and pseudopotential eigenvalues must be the same. $\varepsilon_l^{PP} = \varepsilon_l^{AE}$.

(ii) The valence pseudo-wavefunction should contain no nodes. This requirement avoids the undesired spatial oscillation associate to the presence of nodes.

(iii) The atomic radial pseudo $R_l^{PP}(r)$ and AE radial $R_l^{AE}(r)$ atomic wave functions with angular momentum *l* must be identical beyond a chosen cutoff r_{cl}:

$$R_l^{PP}(r) = R_l^{AE}(r) \text{ for } r > r_{cl}$$

(iv) The charge enclosed within r_{cl} for the two wave functions must be the same:

$$\int_0^{r_{cl}} |R_l^{PP}(r)|^2 \, r^2 dr = \int_0^{r_{cl}} |R_l^{AE}(r)|^2 \, r^2 dr$$

The last requirement guarantees the transferability of the pseudopotential, by means the independence from the chemical environment. Several pseudopotential recipes have been proposed [111-113]. In our calculation we follows the implementation of Troullier and Martin [114]. These pseudopotentials are accurate also for atoms for which the use of previous pseudopotential was restricted, like first row atoms, transition metals and rare earths.

2.3.4 Maximally localized Wannier Functions

The Maximally localized Wannier functions provide a vivid representation of chemical concepts such as covalent bonds and electron lone pairs [115]. The Wannier functions $w_n(\mathrm{r} - \mathrm{R})$ are a localized representation alternative to Block orbitals of the electronic states in a solid. The labeling follows the lattice vector of the unit cell **R** instead that the wave vector **k**.

They are defined via a unitary trasformation of the Block function $\psi_n^{\mathbf{k}}(\mathbf{r})$. The Wannier function assiciated with band *n* are written as:

$$w_n(\mathbf{r}-\mathbf{R}) = \frac{V}{(2\pi)^3}\int d\mathbf{k} e^{-i\mathbf{k}\cdot\mathbf{R}}\psi_n^{\mathbf{k}}(\mathbf{r})$$

The arbitrariness in the phase factor of each Block orbital is reflected in the non-uniqueness of the Wannier orbital definition. In the more general definition for a composite set of bands a unitary transformation that mixes bands and wave vectors can be applied to obtain new sets of orbitals.

Between all the possible sets of localized orbitals Marzari and Vanderbilt [115] basis that minimizes the total spread of the Wannier orbitals, given by the functional:

$$\Omega = \sum_n \left(\left\langle \mathbf{r}^2 \right\rangle_n - \left\langle \mathbf{r}_n \right\rangle^2 \right)$$

The centers $\left\langle \mathbf{r}_n \right\rangle$ of the maximally localized Wannier orbitals obtained with this procedure have the properties of providing an immediate picture of electron localization. They could also provide quantitative [116,117] as well as a pictorial description of chemical bonds. For instance, in the ethylene C=C bond [115] the two associated centers are out of the plane of the molecule, as the Lewis picture of the double bonds suggests.

3 Systems and computational details

We performed simulations using classical molecular dynamics and DFT calculations. Simulated structural models differed from number of K^+ or Na^+ ions, protonation states of tritable side chains, and water content inside the cavity. In the next two sections we report the general procedure we followed to build the structural models and the parameterization used. The list of all the simulations performed is reported in section 3.3, where we is also notified, when necessary, differences from the scheme described in 3.1 and 3.2.

3.1 Structural models

Models for MD calculations. Our structural model was based on the structure of the KcsA potassium channel described in § 1.4.2 [8]. Part of the side chains of five amino acids (Arg27, Ile60, Arg64, Glu71, Arg117) missing in the X-ray structure were added using standard residue geometries, taking care to avoid unphysical contacts. The only histidine present in the protein (His25) was assumed to be protonated in the N_δ position, as the latter forms an H-bond to the carbonyl group of Ala109. The missing atoms of the Glu71 side chains were added so as to point towards the NH groups of the Tyr78 backbone [118].

The cytoplasm/membrane environment was mimicked by a water/n-octane bilayer enclosed in a box [82-85]. This approach supplies a stable hydrophilic/hydrophobic liquid interface quickly adaptable to protein geometry, avoiding the stiffness of full phospholipids. The portion of the protein immersed in the organic liquid was comprised between two layers of aromatic residues, which are believed to lie around the two

putative membrane/water interfaces (Fig. 3.1). The total thickness of the octane slab was ~34 Å [8]. Thus, we have immersed this region of the protein between the two layers (namely between Tyr62 and Phe114) in the n-octane solution. The computational schemes used to construct the water/n-octane/water layers, as well as the procedure of immersing the protein into the solvent, are given in next paragraph.

At physiological pH, we can assume that there are 20 positively charged Arg residues and 16 negatively charged residues (12 Glu and 4 Asp). The positive charge of the protein (+4) was neutralized by leaving the C-terminus tail of each chain deprotonated and the N-terminal tail uncharged. Glu71 side chain may be assumed either deprotonated, thus interacting with thyr78 and Gly79, or protonated, sharing a proton with Asp80 and H-binding to Tyr78 [44]. To satisfy these interactions two different side chain were built. Simulations where performed for both models. A different number on K^+/Na^+ ions was added to the system in the different simulations. A variable number of Cl^- counterions were added close to Arg117 and close to Arg27 to balance the charge of added K^+ or Na^+ ions and to neutralize the protein charge in the Glu71 protonated models. The final systems were electroneutral, as required in performing the Ewald summation correctly [98]. The total number of atoms in our models is ~ 30 000.

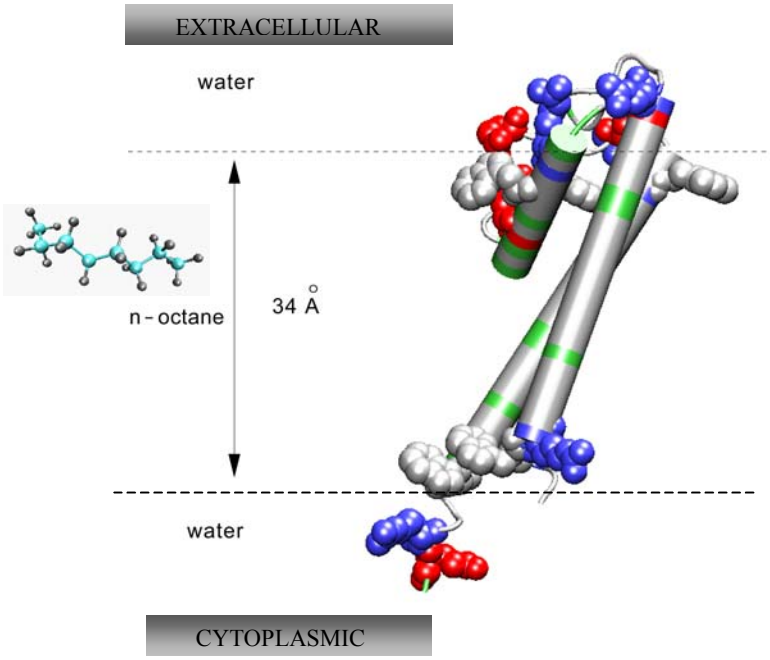

Fig. 3.1 The KcsA structure is immersed in a water/n-octane/water bilayer. The n-octane slab is comprised between the two dashed lines. One protein monomer is represented using hydrophobicity scale for the residue color: gray (hydrophobic), green (hydrophilic), red (negatively charged), blue (positively charged). Aromatic rings at the boundary and charged residues are evidenced by van der Waals representation.

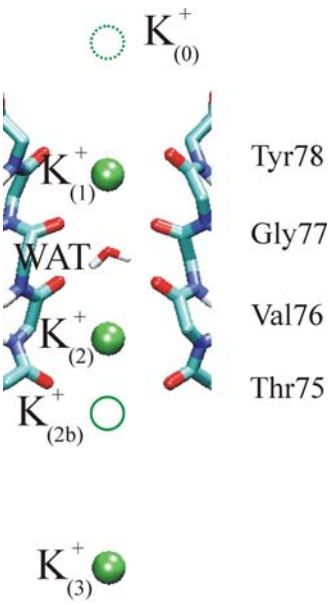

Model name	P	1K	0K	0Na	(0+1)K	(0+2)K	2K	3K
$K^+_{(0)}$	-	-	K	Na	K	K	-	-
$K^+_{(1)}$	-	K	-	-	-	-	K	K
WAT	-	-	-	-	K	K	-	-
$K^+_{(2)}$	-	-	-	-	-	-	K	K
$K^+_{(2b)}$	-	-	-	-	-	K	-	-
$K^+_{(3)}$	-	-	-	-	-	-	-	K

Fig. 3.2 Models used for the MD simulations. Positions along the channel axis are shown in the left panel. The table summarizes the alkali ion positions used in all models. Water molecules were placed in the unoccupied binding sites.

K^+/Na^+ occupy one or more positions illustrated in the left panel of Fig. 3.2. $K^+_{(1)}$, $K^+_{(2)}$ and $K^+_{(2b)}$ are the K^+ binding sites detected in the crystal structure. Two among the three binding sites are supposed to be occupied [8,44]. As initial structure for simulations with two ions into the selectivity filter we chose the $K^+_{(1)}$ and $K^+_{(2)}$ positions (represented as solid spheres in Fig. 3.2) with the crystallographic water molecule WAT in between. Water molecules were put into the filter binding sites when not occupied by an ion. $K^+_{(3)}$ (not present in the coordinate PDB file [8]) is supposed to occupy the water cavity along the channel axis, 8 Å from Thr74 carbonyl oxygens [44]. In some simulations we put an ion in the bulk water along the channel axis in position $K^+_{(0)}$, 6 Å from $K^+_{(1)}$. Table in Fig. 3.2 illustrates the different models. Models **(0+1)K** and **(0+2)K** were built adding an ion in position $K^+_{(0)}$ to the final snapshots of **1K** and **2K** simulations, respectively.

*Potassium Chloride in water***.** A K^+ ion and a Cl^- ion were immersed in a cubic box (≈ 40 Å edge) of Monte Carlo water [119]. At least ten water molecules interposed between the two ions in the starting configuration.

Models for the quantum chemical calculations. We extracted atomic positions from a simulation of KcsA with two K^+ ions inside the selectivity filter (**2K**). At present, it is not possible to calculate the electronic structure of the entire protein with first-principles

methods. Therefore, we focused here on the residues directly binding potassium (Fig. 3.3), namely the backbone ligands of the two binding sites S1 and S2 involved in the translocation. Specifically, the models included: i) the backbone from C(Val76) to N(Gly79) for each of the four subunit. Side-chains were not included in the model; C^{α} atoms and the backbone termini were saturated by hydrogen atoms; ii) the K^+ ion located in binding site S1; iii) two water molecules (WAT1 and WAT2). While WAT2 was already detected in the X-ray structure [8], WAT1 was found to be ordered during the **2K** MD simulation (see results chapter).

Hydrogen atoms were added assuming standard bond lengths and bond angles. The total charge of the model complex is +1.

Eleven snapshots of the MD simulation at room temperature were collected. As initial configuration (frame *f0*) we took the snapshot after 96 ps of dynamics. The subsequent snapshots (frames *f1-f10*) were collected every 5.7 ps.

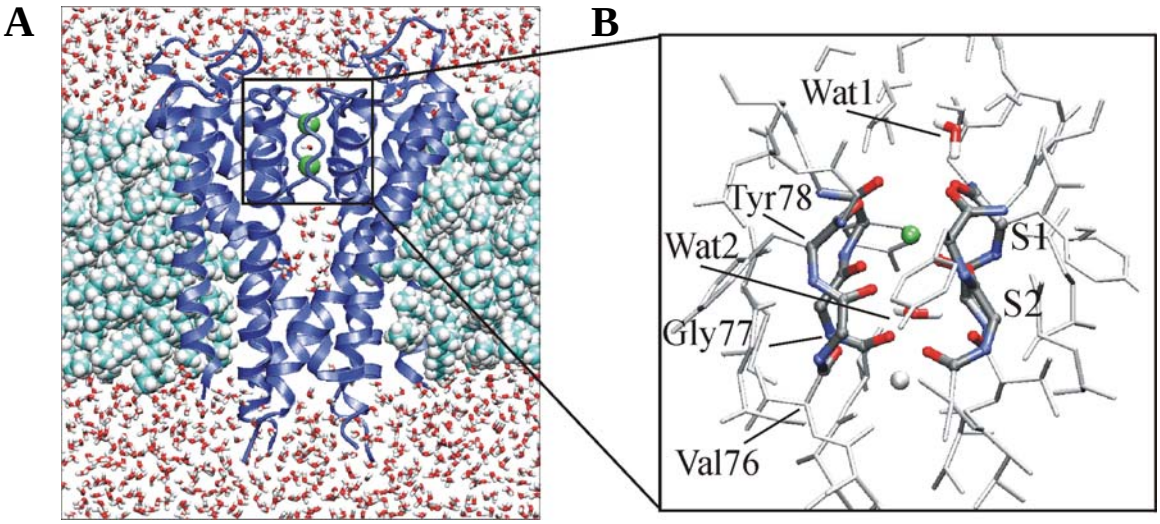

Fig. 3.3 Model used for the quantum chemical calculations. The right panel shows a close up on the selectivity filter in the classical structural model **2K** (left panel). The quantum-mechanical model used in the calculations is drawn with cylinders. Protein hydrogen atoms not shown for clarity. Color palette: C (dark gray), N (blue), O (red), H (white), K^+ (green).

3.2 Computational details

3.2.1 Classical molecular dynamics

Computational setup. All the simulations were carried out with periodic boundary conditions, constant temperature and constant volume. We used the AMBER 5 suite of programs [119].

The temperature was maintained at 298K with the Berensden's thermal coupling [97] using a 0.2 ps separate relaxation time for solvent and solute. The Coulomb interaction was treated using the particle mesh Ewald method [98,99] with ~ 1 Å in charge grid spacing interpolated by 3rd order B-spline and by setting the direct sum tolerance to $5 \cdot 10^{-6}$. The short range electrostatic cutoff was set to 10 Å.

We have used a 10 Å cutoff for the evaluation of the vdW interactions. The SHAKE algorithm [96] has been used to constrain all bonds.

A time step of 1.5 ps was used. The all-atom AMBER force field [92,120]and the OPLS force field [121,122] were used for the protein, the alkali metal ions and n-octane respectively. The water model was the TIP3P [123].

To obtain a structural model of the water/n-octane/water interfaces we considered a box of dimensions $a \times b \times c \sim (65 \times 66 \times 69)$ Å^3 and periodic boundary conditions, then we positioned two slabs of water and octane (respectively 35 and 34 Å in thickness) on the *ab* plane.

The densities of both liquids were adjusted in the starting configuration to the

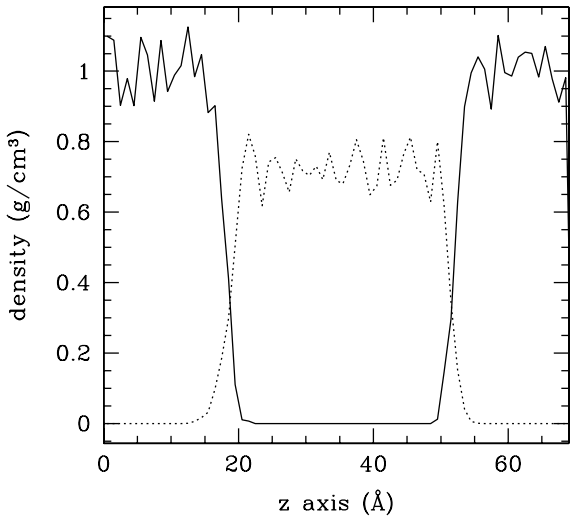

Fig. 3.4 Density profiles of n-octane (dotted line) and water (solid line) along the channel symmetry axis show how the two slabs are well separated.

experimental values. We carried out an NVT-MD run on this system for 0.6 ns. During this time the bilayer has shown a very high stability and the ability to totally drive water out of the hydrophobic region as shown in Fig. 3.4. The final structure obtained has sharp and well-defined hydrophobic/hydrophilic interfaces where the KcsA starting structure will be located.

Inserting a channel protein in a membrane is not trivial, but our model membrane allowed us to use a simple procedure. We estimated the volume of the protein in the hydrophobic and hydrophilic regions by calculating the Connolly surfaces [124] in the two regions (see Fig. 3.1). We then eliminated water and octane molecule consistently with the calculated volumes and with the bulk experimental densities.

Finally, we located the crystallographic water molecule and 29 other water molecules into the channel pore by calculating again the internal Connolly volume. In some simulations we also used a larger amount of water as reported in section 3.3.

To equilibrate the solvent around the protein, we used the following procedure:

i) 40 ps of MD for the water molecules keeping the protein and the n-octane fixed; ii) 40 ps of MD keeping the rest fixed; iii) full relaxation of the water and n-octane solvent for another 200 ps of MD.

All the structural models exhibited a good Ramachandran plot with no residues in outlying regions [125].

After energy minimization, the structures were heated up to 298 K by 15ps long MD runs performed at 20, 50, 100, 150, 250, and 298 K using Berendsen's thermal bath (2.1.4).

Calculated Properties. (i) Root mean square displacements. (ii) Radial g(r) and angular g(θ) distribution functions (dfs). Water $g(\theta_{OH\text{-}O})$ was calculated up to d(H-O) = 2.5 Å, that is the distance corresponding to the first minimum of $g(r_{O\text{-}H})$ in bulk water [123]. (iii) K^+ coordination numbers were calculated by integrating $g(r_{K^+\text{-}O})$ up to its first minimum at 3.65 Å [126]. In simulations performed on **3K** models these numbers take into account also the coordination bond with Thr75 carbonyl oxygens, which turned out to replace up to four water molecules for ≈ 35% of simulated time. (iv) Pore radius profile was calculated with the HOLE program [127]; its integral provided the pore volume. (v) The water electric dipole was calculated from the TIP3P water model

partial atomic charges [123]. (vi) In **3K** simulations (see results chapter), calculations of electric fields along the channel axis for a) the protein-$K^+_{(1)}$-$K^+_{(2)}$ adduct and b) the four pore helices (residues 62-74) were based on RESP partial atomic charges [92]. A simple point charge model *in vacuo* (dielectric constants $\varepsilon = 1$) as well as the Poisson-Boltzmann model [101,102] ($\varepsilon = 78$ and $\varepsilon = 2$ for water and for the protein, respectively) were used. In model b) all charges other than the pore helices atoms were turned off. (vii) In **3K** simulations (see results chapter) $K^+_{(2)}$/Water and $K^+_{(2)}$/$K^+_{(3)}$ electrostatic interaction energies were calculated during the dynamics every 6 ps using the same simple point charge model as above. Thr75 side chain, which has been shown solvating frequently $K^+_{(3)}$ (see (iii)) was considered in this calculation as belonging to the cavity solvent.

Molecular structures were drawn using the Cerius2 [128] and VMD program [129].

3.2.2 DFT calculations

Computational details. The quantum problem is solved within first principles density functional theory [104], in the formulation by Kohn and Sham [105] and within the local density approximation with gradient correction. The exchange and correlation functional used were those from Beche [107], and Lee, Yang, and Parr [108], respectively. The core-valence electron interaction was described using Martins and Troullier pseudopotentials [114]. The systems were treated as isolated [110]. The Kohn and Sham orbitals were expanded in a plane wave basis set up to an energy cutoff of 70 Ry.

The electronic wavefunction was optimized up to a gradient less than $5 \cdot 10^{-7}$ a.u.

Calculated properties. (i) Potassium-oxygen radial distribution functions ($g(r_{K^+\text{-}O})$) were calculated as in ref. [89]. Integration of $g(r_{K^+\text{-}O})$ provides an estimate of K^+ coordination number. The integral was calculated from zero to its first minimum in bulk water (r_{K^+}-O=3.65 Å [126]) . (ii) The electron density difference $\Delta\rho$, has been calculated by subtracting the densities of the metal ion and the ligands from the density of the complex: $\Delta\rho = \rho_{model} - \rho_{ion} - \Delta\rho_{ligands}$. The charge difference Δq of an atom was calculated as an integral of $\Delta\rho$ on a sphere centered on atom within a cutoff r_{cut}. (iii) The centers of the maximally localized Wannier orbitals were calculated as in ref. [115].

3.3 Molecular dynamics calculations

Based on the models illustrated in section 3.1 (see also Fig. 3.2) we have performed the MD simulations summarized in the following table:

Structural model	**Structural details**	**Computational details**	**Simulated time**
P	Not protonated Glu71.	Time step 1fs, short range cutoff 8Å.	0.7 ns
1K	"	"	1.5 ns
R89C	Same as 1K but with R89C mutation.	"	0.7 ns
(0K), (0Na)	Not protonated Glu71. The position of the alkali metal ion in $K^{+}_{(0)}$ was first constrained during thermalization.	"	0.3 ns
(0K), (0Na)	Same as previous simulations but without constraints.	"	"
(0+1)K	The last snapshots of simulation 1K was taken as initial structural model.	"	"
3K	Protonated Glu71. Simulations with different water content (30 or 50 molecules) were performed.	Time step 1.5 fs, short range cutoff 10 Å.	2.0 ns
2K	"	"	0.5 ns
2K	Same as previous simulations but constraining the filter ions for the first 0.13 ns.	"	0.5 ns
3K	Same as previous 3K simulations but with Glu71 not protonated.	"	"
(0+2)K	The last snapshot of 2K simulation was taken as initial structural model. $K^{+}_{(0)}$ was constrained for the first 0.2 ns.	"	1 ns

4 Results and discussion

In this chapter we presents results from our research work on the K^+ channel [130-132].

We first report general dynamical features of the protein that are common to all classical simulations (section 4.1). In section 4.2, we discuss about the structural role of a previously unrecognized inter-subunit salt bridge. In section 4.3, the properties of the outer (extracellular) mouth of the channel will be investigated as well as the binding differences between Na^+ and K^+ ions. The stability and dynamical properties of the potassium ions in the binding sites and of the water molecules into the pore will be investigated in section 4.4. Section 4.5 we report an *ab initio* study of the K^+-protein interactions during the potassium permeation through the selectivity filter of the channel. Finally, in section 4.6, our results are compared to those found by other theoretical works on KcsA appeared in literature in the last two years.

4.1 General features

The features reported in this section refers to **1K** [130], 3**K** [131] and to **P** models. Many general features found for **3K** are common to all the wild-type MD simulations.

4.1.1 Simulations with ions bound

During the dynamics **(3K)**, the structure of the K^+-protein complex was stable. After 0.6 ns, and for the rest of the simulations (up to 2 ns) atoms of the protein fluctuated with a root mean square displacement (rmsd) of 2.7 ± 0.1 Å (2.1 ± 0.1 Å for backbone atoms). These values were not affected by differences in water content into the cavity as

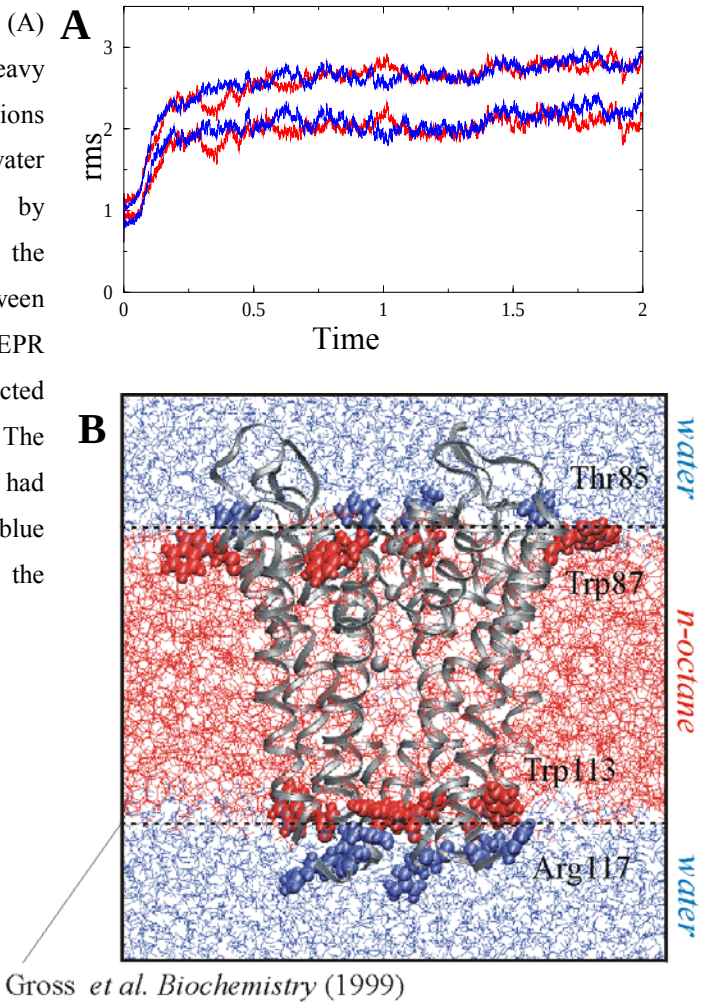

Fig. 4.1 Overall dynamics. (A) Backbone atoms (lower lines) and heavy atoms (upper lines) rms for **3K** simulations with 30 (red) and 50 (blue) starting water molecules. The rms was calculated by fitting the evolved structure with the minimized one. (B) Comparison between our protein-octane-water system and EPR structural data of KcsA in reconstructed phospholipid bilayers [10]. The hydrophobic/hydrophilic interfaces had been indicated to lies in between the blue and the red colored residues, around the dashed lines.

the data with 30 (red lines) and 50 (blue lines) starting water molecules show in Fig. 4.1A.

An analysis of the deviations from the starting and the evolving structures revealed that residues forming the channel turret (from 52 to 61) experienced fluctuations three times larger than those lining the selectivity filter (residues 75-79). The relatively high stability of the selectivity filter may be a physical feature relevant for ionic selectivity [64].

The secondary structure of the 12 α-helices remained stable throughout the simulations, with the hydrogen bonds along each backbone well maintained.

The n-octane/water interfaces were well preserved in all dynamics. The protein location with respect the octane bilayer turned out to be in excellent agreement with

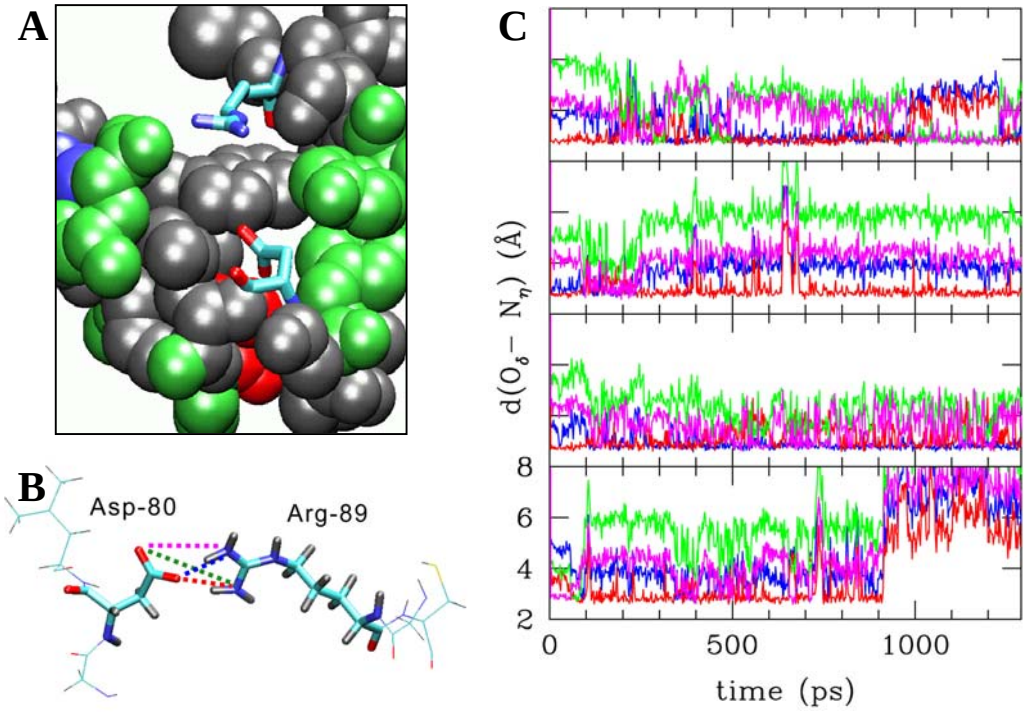

Fig. 4.2 (A) Asp80 and Arg89 in the crystal structure. Redisues in ball representation are colored by hydrophobicity scale: gray (hydrophobic residues), green (hydrophilic), blue (positively charged), red (negatively charged). (B) View of the Asp80-Arg89 salt bridge and (C) corresponding carboxylate oxygen-guanidinium nitrogen distances plotted as a function of time. Distances are plotted for the four Asp80 - Arg89 pairs.

recent EPR data which followed our set up. Indeed, the membrane hydrophobic/ hydrohilic interfaces indicated by Gross *et. al* (dashed lines in Fig. 4.1B) [10], are well mimicked by our membrane model.

In model **1K,** the starting position of the potassium ion turned out not to be stable since the thermalization run at 20 K. The ion quickly occupied the crystallographic water position (WAT binding site), about 4 Å away from the starting point in the inner direction, and remained there for the remainder of the simulation.

Probably this instability is due to the different binding sites of the channel when the selectivity filter is occupied by one ion instead of two (as in the X-ray structure).

4.1.2 Simulation without ions bound

A simulation in the absence of a K^+ ion in the binding site (**P** model) also underlined the important role of the metal ion for protein stability [133,134]. Indeed, the selectivity

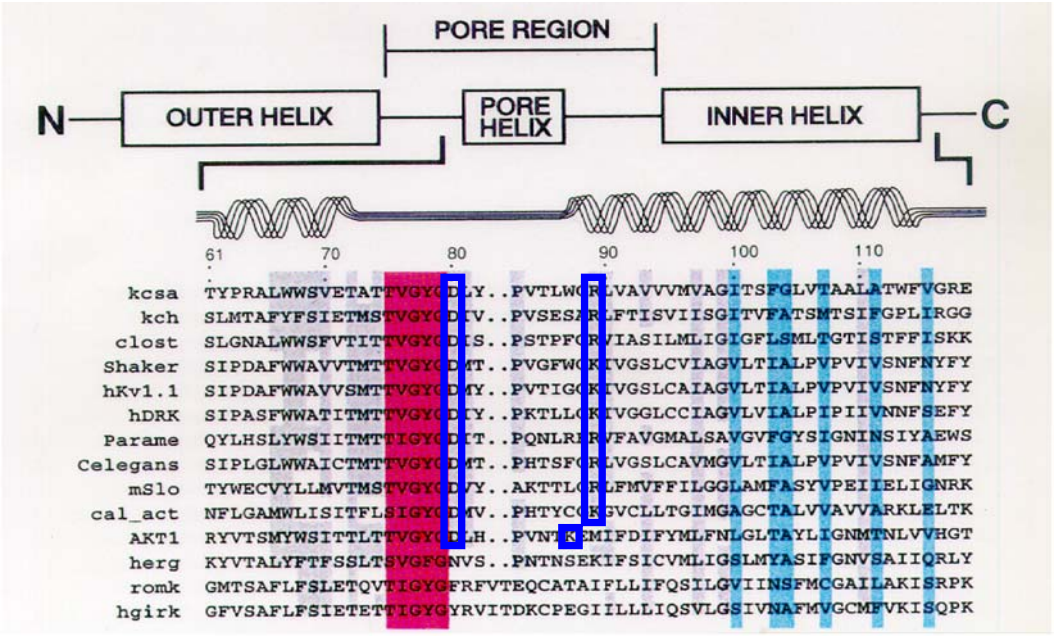

Fig. 4.3 The KcsA Asp80/Arg89 salt bridge is conserved in K^+ channel family sequences. The pairs of homologous residues are highlighted in blue. Figure adopted from ref. [8].

filter region backbone (from Tyr75 to Gly79) of the KcsA channel, without a K^+ inside, experienced larger mobility than that of the KcsA channel with a K^+ ion in the inner pore (rms fluctuations were (1.9 ± 0.5) Å and (1.0 ± 0.3) Å, respectively).

4.2 A previously unrecognized inter-subunit salt bridge

The following section is based on simulations performed on **1K** wild type and R89C mutant models [135]. The quaternary structure of the channel was stabilized by the formation of salt bridges between the Arg89 and Asp80 in neighboring subunits, not evident in the X-ray structure (Fig. 4.2A) nor recognized by crystallographers [8]. Some of these salt bridges broke and formed on the ns time scale Fig. 4.2B,C. Force field based calculations [92] showed that these salt bridges are very important for the integrity of the quaternary structure as they account for approximately half the total subunit-subunit association energy.

The proposed role of these two residues agrees with the observation of structural similarity between the KcsA channel and eukaryotic K^+ channels [43] and with conservation of these residues in a variety of K^+ channels as shown in Fig. 4.3.

To further explore the Asp80-Arg89 induced subunit-subunit stabilization, a simulation where Arg89 was mutated into a cysteine (R89C mutant) was performed. The calculation mimicked the experiment of E. Perozo *et al*. [40], which showed that this mutation essentially abolishes protein expression in KcsA channel. Analogous mutations in other K^+ channels revealed a similar loss of functional expression: D378T and D378C in *Kv2.1* [27,28], K456D in *Shaker* [136]. After a few hundred ps, the quaternary structure of the mutant lost its original conformation (Fig. 4.4A) and the selectivity filter became wider (Fig. 4.4B).

The conclusions might be more general, because the presence of the salt bridge we proposed [135] has been observed in a variety of different systems in our simulations (i.e **2K** and **3K**) and in simulations reported by other authors [70,72,131]. Calculations performed with the protonated form of Glu71 (**3K** model) also confirmed the formation

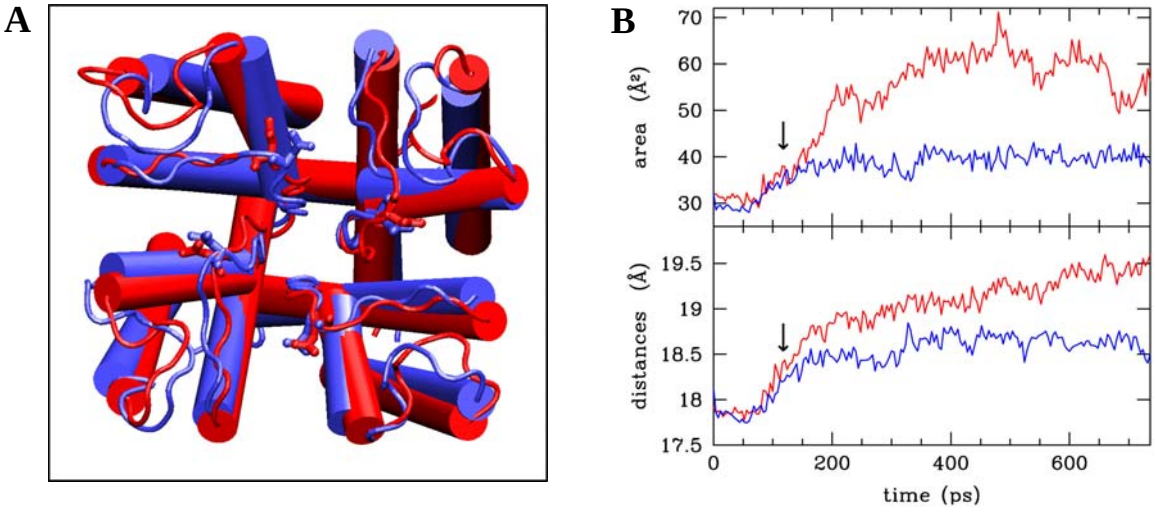

Fig. 4.4 Molecular dynamics of the KcsA (blue) and its R89C mutant (red). (A) Comparison between the two structures after 450 ps (α-helices indicated as cylinders). (B) Selected geometrical features as a function of time. Bottom: average distances between the center of mass of the four subunits. Top: pore area of the four subunit pore walls (residues from 76 to 79). The mutant channel exhibits a larger drift than the wild type KcsA channel. The arrow indicates the time when thermalization at 298 K was achieved.

of the salt bridges [131]. During these dynamics, Asp80 maintained its H-bond with protonated Glu71, the average O_δ(Asp80) – O_δ(Glu71) distances in the four subunits ranging from 2.6(1) to 2.8(2) Å.

Our calculations therefore suggest that the loss of the functional expression of K^+ channels where the aspartate and/or the arginine (or lysine) residues near the external vestibule were mutated [27,28,40,136] was due to a partial disruption of the quaternary structure and of the selectivity filter.

After our work [135], the structural function of the salt bridge was further investigated by mutagenesis experiments [137], that revealed its role in the stability of the outer mouth structure.

4.3 Ion dehydration in the outer mouth

The dehydration process seems to be a fundamental step for the binding and selectivity properties of K^+ channels (see § 1.5.1, 1.5.2). The metal binding to the protein was studied by locating K^+ or Na^+ ions in the bulk water at the outer vestibule of the channel. Simulations with different number of K^+ ions in the selectivity filter binding sites were performed (models **0K**, **0Na**, and **(0+1)K** in § 4.3.1**,** model **(0+2)K** in § 4.3.2).

4.3.1 Potassium and sodium binding

The electrostatic potential energy of the protein (calculated with the Poisson-Boltzmann equation [101,102]) was significantly negative in the channel vestibule and close to the first binding site (Fig. 4.5A). The energy profile turned out to be very similar in the presence or absence of a potassium ion in the $K^+_{(2)}$ binding site. Thus the KcsA channel attracts cations and repels anions from its inner pore.

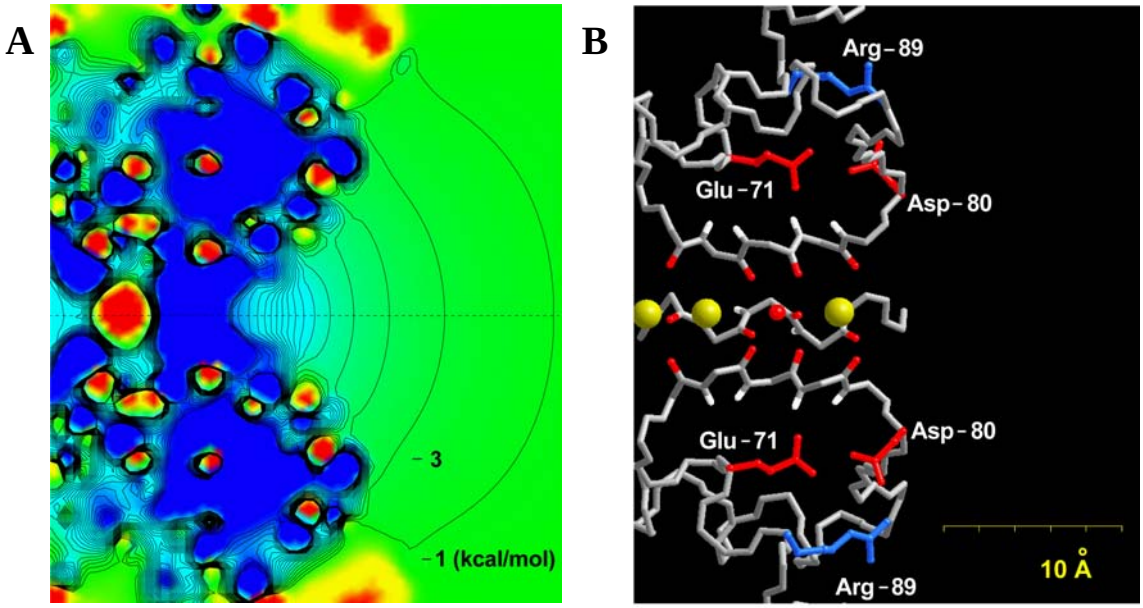

Fig. 4.5 Electrostatic energy profile in the outer mouth of the KcsA channel. (A) Electrostatic potential energy [101,102] in the pore and solvent regions through a planar section containing the channel axis. The initial configuration of the KcsA channel was used with a potassium ion in the second binding site. Black lines indicate isoenergy contours at a 2 kcal/mol separation. Red (blue) indicates a very positive (negative) electrostatic energy and therefore cation repulsion (attraction). (B) The structure of some residues contributing to the electrostatic energy profile in A. The three yellow spheres indicate the three binding sites. The first binding is the more external. The small red sphere is the oxygen of the crystallographic water molecule. Backbone oxygens (red) and the amide hydrogens (white) in the selectivity filter of three subunits. Asp80 and Glu71 of two opposing subunits (red) and two Arg89 of the two other subunits (blue). Diagrams in A and B are on the same scale.

Our electrostatic energy analysis [92,101,102,119,120,122,123,138] also showed that this valence selectivity was largely caused by the external ring of Asp80 and the inner ring of Glu71 (Fig. 4.5B). The ring of positively charged Arg89 (Fig. 4.5B), located more distant from the channel axis, reduced but not abolished the attraction of cations. When a potassium ion was in the first binding site $K^+_{(1)}$, the electrostatic potential energy in the channel vestibule was less negative.

The metal binding to the protein was studied by locating hydrated K^+ or Na^+ ions in the outer vestibule. Simulations carried out with and without a potassium ion into the pore led to similar results. At the beginning of the simulations (models **0K**, **0Na)** ions were located in the bulk solvent (at 6 Å from the pore region) and were coordinated by

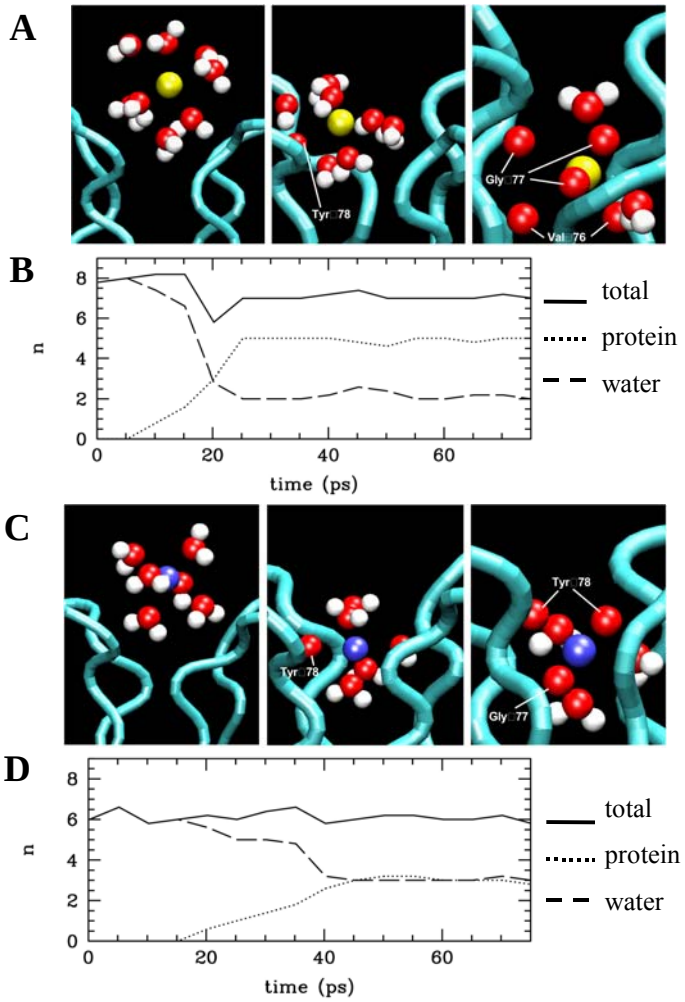

Fig. 4.6 Binding of Na^+ and K^+ to the channel. Selected snapshots ((A): after 2 (left), 16 (middle), and 60 (right) ps; (C): after 2 (left), 24 (middle) and 60 (right) ps) are shown for both K^+ (A) and Na^+ (C) cations: ions are completely hydrated in the outer mouth of the vestibule (left), interact with the protein (middle) and diffuse into the first binding site (right). Coordination numbers (n) of K^+ (B) and Na^+ (D) plotted as a function of time. n is calculated assuming K^+- (Na^+-) ligand cutoff of 3.65(3.25) Å [126]. Total coordination numbers (solid line) and contributions from the solvent (dashed) and from the backbone (dotted line) are reported.

six (Na^+) or eight (K^+) water molecules (first panels of Fig. 4.6A and C). Both ions diffused within a few tens ps towards the first binding site (second panels of Fig. 4.6A and C) and lost part of their hydration shell (Fig. 4.6B and D). Diffusion occurred in the absence of any external driving force. K^+ was coordinated to two water molecules and to the backbone carbonylic oxygen atoms of Gly77 and Val76 (last panel of Fig. 4.6A). Na^+ was coordinated to three water molecules and to the backbone oxygen atoms of Gly77 and Tyr78 (last panel of Fig. 4.6C). Thus potassium was coordinated to less water molecules than sodium and entered deeper into the channel inner pore.

As the selectivity filter has larger fluctuations in the absence of K^+ in its inner pore, the exact number of water molecules coordinated to the ions depended on the time during which the inner pore remained empty (but on average more water molecules

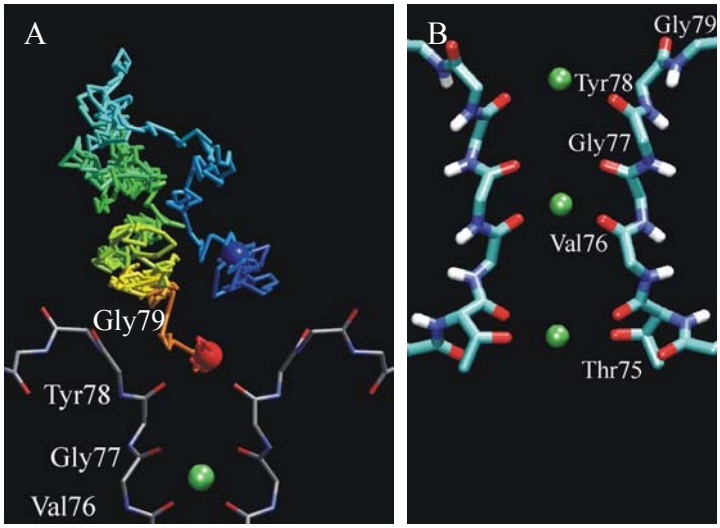

Fig. 4.7 (A) Ion trajectory from **(0+2)K** simulation is represented by the colored trace. $K^+_{(0)}$ diffused from the bulk water (blue sphere) to the new binding site (red sphere) in 400 ps. The average position of the $K^+_{(1)}$ potassium ion in the WAT binding site is also represented by a green sphere. (B) Average positions of the ions superimposed to the crystal structure.

remained bound to Na^+ than to K^+). The different hydration state of Na^+ and K^+ in the channel inner pore seems to be a basic factor determining ionic selectivity [64].

4.3.2 Can the pore accommodate three ions?

The binding of a K^+ ion from the outer mouth to the selectivity filter was studied in a configuration containing two ions into the filter (**(0+2)K** model). As shows in Fig. 4.7, the ion widely diffused into the extracellular solution before binding the Tyr78 backbone oxygens. The ion remains in this non-crystallographic binding pocket during the rest of the simulation (up to 1ns) as well as the other two ions presents into the filter. The measured coordination numbers of the protein ligands (3.8(0.5)) and of the water (3.6(0.6)) turned out to be very similar, indicating that in this binding site the ion is only partially dehydrated. Three ions and two water molecules can, therefore, accommodate into the selectivity filter at the same time in a configuration that is stable in the time scale investigated.

The dehydration capability of the KcsA channel that we found in the previous section seems to be extendible to the case where the filter is already doubly occupied. Further crystallographic studies [139], using different ionic strength, might reveal if this belongs or not to the K^+ permeation pathway.

4.4 K^+ and water dynamics

The structural and dynamical properties of water in confined pores are a crucial issue for understanding the ion-ion interactions and the permeation mechanisms in ionic channels (§ 1.5.3). In this section we investigate the dynamical properties of the three potassium ions presents in the crystal structure as well as the water molecules into the hydrophobic cavity (model **3K**). A comparison with a simulation without the cavity ion $K^+_{(3)}$ is also reported (model **2K**).

During the **3K** simulation[3], the channel structure is rather stable: indeed α-helix hydrogen bond patterns as well as subunit-subunit contacts are well preserved in the ns time scale. Structures sampled every 0.15 ns exhibit a fairly good Ramachandran plot [125][4]. The protein is also well equilibrated. After ≈ 0.6 ns, the rmsd fluctuates around the average value of 2.7(1) Å (2.1(1) Å for backbone atoms).

The geometrical properties of the channel pore can be described by the pore radius profile [127]. The MD-averaged pore radius belonging to the region occupied by internal water and K^+ is very similar to that of the X-ray structure [8]. Consistently, the volumes, calculated over these regions, are rather similar (397 $Å^3$ and 486 $Å^3$, for the MD and the X-ray structure, respectively).

Thus, force-field parameterization used in this work appears to reproduce well the structural features of the protein.

Mobility of the potassium ions. The three K^+ ions remain in their initial binding sites in the ns time scale investigated (Fig. 4.8). However, their mobility is markedly different: $K^+_{(1)}$ and $K^+_{(2)}$ experience small fluctuations around their average positions (the rmsd's along the channel axis = 0.3 Å for both ions). In contrast, $K^+_{(3)}$ is very

---

[3] Simulations **3K** carried out with different number of water molecules (30 and 50) turned out to give a similar water content at the end of the simulations (see further in text) as well very similar results. For sake of simplicity we reported here only the molecular dynamics **3K** performed with 30 water molecules, and therefore, for comparison, the molecular dynamics **2K** with 31 water molecule (see § 3.1 and § 3.3 for further datails).

[4] In one subunit**,** Val76 backbone rearranges after ≈ 0.1 ns to a different conformation, which also exhibits a good Ramachandran plot [125] (From φ,ψ = -122, -25 to φ,ψ = -127, 141). As a result, WAT replaces Val76 carbonyl group in the coordination sphere of $K^+_{(2)}$ for the rest of the simulation.

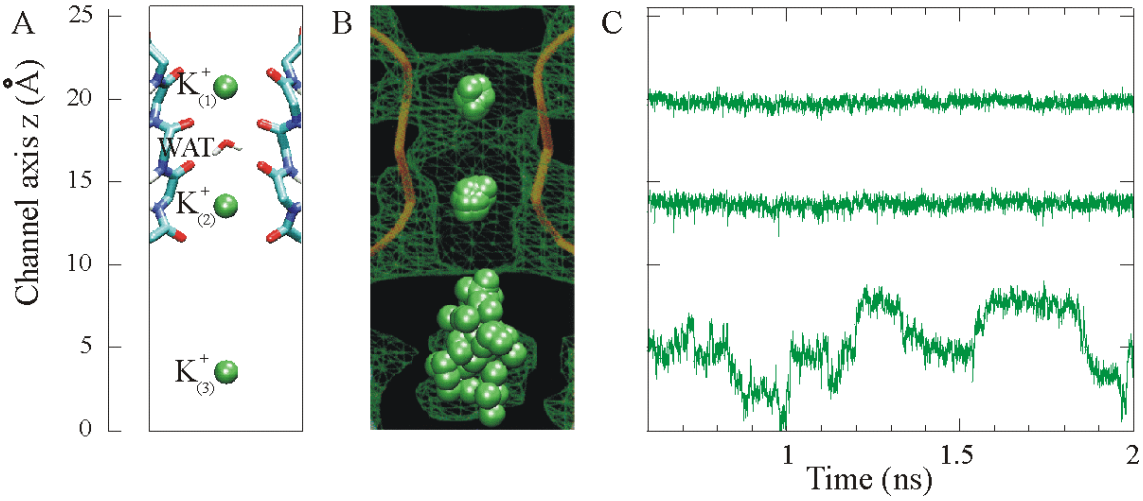

Fig. 4.8 Structure and mobility of potassium ions (green). (A) Location and labeling of the ions and of the crystal water. The position along the channel axis is also shown. The origin is set arbitrarily. (B) Scatter plot of K^+ positions during the production dynamics displayed every 50 ps. The experimental density map (1 σ contoured) and the backbone trace (yellow) are also displayed from reference [8]. (C) Ion motion on the channel axis plotted as a function of time.

mobile (rmsd 1.9 Å), its ensemble of positions being fully consistent with the diffuse experimental electronic density inside the channel cavity [8].

$K^+_{(3)}$ is highly hydrated. However, it spends a significant portion of the simulated time binding also to some or all of the four Thr75 O_γ oxygen atoms. Comparison of the MD-averaged coordination number (6.8(0.9)) with that of KCl in bulk water (6.9(1.0)) shows that the potassium coordination shell is similar to that of potassium in water.

Internal hydration of the channel. While WAT maintained its position during the dynamics, five water molecules left the channel cavity during the system equilibration, and diffused toward the hydrophobic layer and bulk water within 0.2 ns. Water diffuses to a greater extent if a larger water content is initially present in the channel cavity. As a result, a similar number of waters was present at the end of both dynamics (2 ns). Thus, the channel appears to accommodate between two and three tens of water molecules inside the cavity.

Water structural properties are conveniently compared to those of bulk water through

analysis of g_{OO}, g_{OH} radial and $g_{OH\text{-}O}$ angular distribution functions (dfs). While the radial dfs are barely similar, small but significant discrepancies are found between the two $g_{OH\text{-}O}$'s: the channel water $g_{OH\text{-}O}$ is broader and exhibits a smaller maximum than that of the bulk. Visual inspection of the water network confirms that water in the cavity is structured differently from the bulk water. A typical MD snapshot (Fig. 4.9A) shows that the water c_2 symmetry axes are partially aligned along the axis channel (z coordinate).

An important consequence of this alignment is the formation of a large dipole **D** directed essentially along the z-axis (see Fig. 4.9A). **D** points towards the extracellular side during most of the simulation, although it experiences large fluctuations. Fig. 4.9B shows that the z component (D_z) oscillates from more than 30 Debye to zero and even to negative values, which means **D** pointing toward the intracellular side (Fig. 4.9B).

Water molecules are not polarized uniformly in the cavity. The largest polarization is found in the region close to the extracellular side (Fig. 4.9C). There, the dipole/molecule contribution along the z axis reaches 2.0 Debye, that is ≈ 85% of TIP3P water dipole [123].

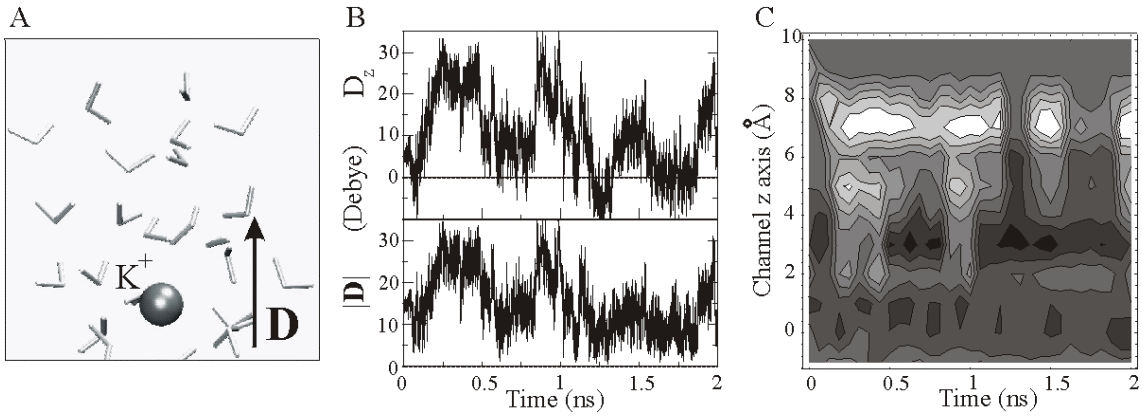

Fig. 4.9 Electric dipole momentum of the water inside the channel. (A) Representative snapshot of water polarization at 0.9 ns. (B) The inner water total dipole |**D**| and its component along the channel axis D_z plotted as a function of the simulated time. Almost all contribution to |**D**| arises from D_z. (C) D_z fluctuations during the dynamics are plotted as a function of channel axis and simulated time. Lighter regions correspond to D_z orientation towards extracellular side. Contours range from -2 Debye/Å (black) to +5 Debye/Å (white). Scale of the z axis is consistent to the that shown in Fig. 4.8.

What are then the important factors responsible for the strong water polarization and of its large fluctuations in time?

Inspection of crystal and MD structures points to the four pore helices as key factors for *water polarization*, as their COOH termini point toward the channel cavity from the

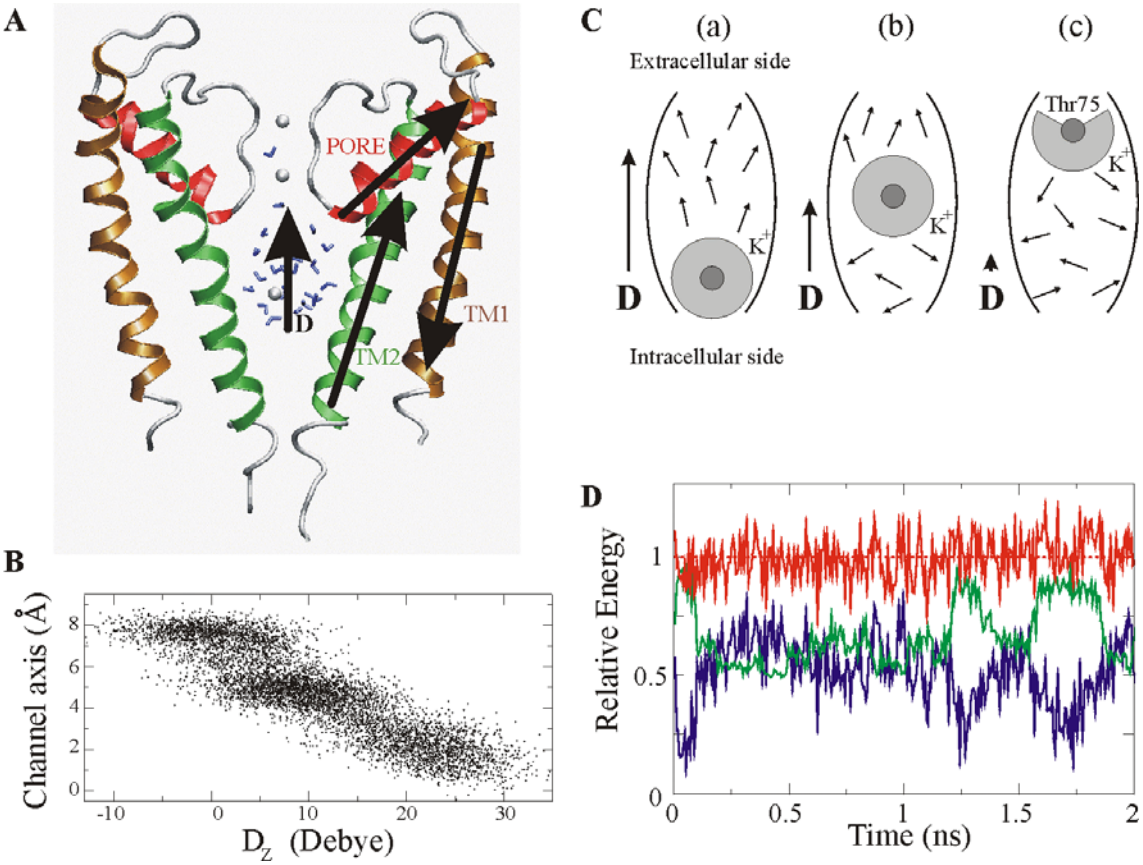

Fig. 4.10 (A) Water/helices dipole-dipole electrostatic interactions. Dipole momenta are sketched as black arrows. The role of the pore helix for water polarization is apparent from the relative orientation of **D** and the helix dipoles (B) Correlation plot between water dipoles D_z and the $K^+_{(3)}$ positions along the axis channel. The scale of the axis is consistent with Fig. 4.8 and Fig. 4.9. (C) Interplay between $K^+_{(3)}$ dynamics and water polarization inside the cavity. Each cartoon includes water single (thin arrows) and total (thick arrow) **D** dipoles as well as $K^+_{(3)}$ and its first hydration shell (dark and light gray spheres, respectively). **D**, large and directed towards the extracellular side in (a), decreases dramatically when $K^+_{(3)}$ moves to the center (b), becoming small or negative when the ion is located in the top (c) of the cavity. When $K^+_{(3)}$ is located close to the extracellular side (c), it can bind to Thr75 Oγ atoms (average coordination number 2.6(0.9)). (D) Electrostatic force field based interaction energies between $K^+_{(2)}$/ and the ($K^+_{(3)}$-water) systems in the channel cavity. $K^+_{(2)}$/cavity (blue), $K^+_{(2)}$/$K^+_{(3)}$ (red), and $K^+_{(2)}$/inner water (green) energies are plotted as a function of simulated time. Energy values are expressed in units of average $K^+_{(2)}$/cavity interaction (65 kcal/mol).

extracellular side [44] (Fig. 4.10A). Electrostatic calculations, based either on a simple point charge model (PC) or on the Poisson-Boltzmann equation (PB) [101,102], show that the helix field accounts for more than three quarters of the field of the protein, with a magnitude of the order of ten (PB) to one hundred (PC) mV/Å. Furthermore, the field increases on approaching the extracellular side of the channel, consistently with the polarization plot shown in Fig. 2C.

The electrostatic modeling also shows that the two transmembrane helices TM1 and TM2 do not provide a significant contribution to water polarization. Indeed, their effect almost cancels out, because their large dipoles have antiparallel orientation (Fig. 4.10A).

The *large fluctuations* of the total water dipole must arise from large rearrangements or fast motions of interacting groups. In this respect, $K^+_{(3)}$ is putatively important because of its high mobility inside the cavity. That this is indeed the case is shown by the strong correlation between the ion position along the channel z axis with D_z magnitude (Fig. 4.10B). Three regimes can be identified: when $K^+_{(3)}$ is close to the extracellular side ($z > 6$ Å, scale from Fig. 4.8, Fig. 4.9, and Fig. 4.10B), D_z is zero or even negative (Fig. 4.10B, upper region); instead, when $K^+_{(3)}$ is located near the intracellular side ($z < 4$ Å), D_z is positive and very large (Fig. 4.10B, lower region); finally, when $K^+_{(3)}$ is found in the center of the cavity ($4 \leq z \geq 6$ Å), D_z assumes intermediate values (Fig. 4, middle region).

An explanation of the dynamic influence of $K^+_{(3)}$ on water polarization is offered by its hydration properties. Although the *first* hydration shell of $K^+_{(3)}$ provides essentially a zero net contribution to **D**, the *outer-sphere* hydration properties do affect water polarization (Fig. 4.10C). When $K^+_{(3)}$ is located at the bottom of the cavity, it tends to orient all the water dipoles but those directly bound towards the extracellular side (Fig. 4.10C(a)). Thus, the net effect of $K^+_{(3)}$ adds to that of the pore helix dipoles, and **D** is very large. When $K^+_{(3)}$ moves towards the cavity center, its polarization effects are approximately isotropic also on the outer-shell spheres, as in bulk water. Thus, it provides a negligible contribution to water polarization**.** As a consequence, **D** is considerably smaller but still significant because the pore helix field (Fig. 4.10C(b)). Finally, when $K^+_{(3)}$ is located near the extracellular side, it tends to polarize the water

dipoles so as to counterbalance that induced by pore helix dipoles, leading to a dramatic reduction of **D**. The net result is that water *is not* polarized in the channel cavity (Fig. 4.10C(c)).

In summary, the pore helix dipoles generate the electric field responsible for the strong water polarization, which fluctuates widely because of the high mobility of the potassium ion inside the cavity.

These findings can provide a rationale for the stability and the relatively low mobility of two potassium ions in the binding sites. Because **D** points towards $K^+_{(2)}$, the electrostatic interaction between $K^+_{(2)}$ and the potassium/water system is expected to be *repulsive* and therefore might prevent $K^+_{(2)}$ (and hence $K^+_{(1)}$) to diffuse inside the channel. Indeed, the calculated $K^+_{(2)}$/cavity interaction energy is positive and much larger than kT (of the order of several tens kcal/mol). Exact values must be taken with caution as they are based on a simple force field calculations. Furthermore, it is almost *constant* over the entire simulation (Fig. 4.10D). This result is apparently surprising because $K^+_{(3)}$ fluctuates very widely in the channel cavity (its motion along the axis channel ranges over 7 Å). However, because of the correlation between $K^+_{(3)}$ position and water polarization (Fig. 4.10B,C), the $K^+_{(2)}/K^+_{(3)}$ and the $K^+_{(2)}$/water interaction energies compete to each other. When $K^+_{(3)}$ is close to $K^+_{(2)}$ (top of cavity channel, Fig. 4.10C(c)), it provides most of the electrostatic repulsion. In contrast, when $K^+_{(3)}$ is far from $K^+_{(2)}$ (Fig. 4.10C(a)), ion-ion repulsion is drastically reduced and **D** provides a fundamental contribution to the repulsion energy.

Would this dynamical equilibrium of the channel be broken if one of the ingredients were missing? To answer this question, we follow the dynamics of a system in which $K^+_{(3)}$ is removed. MD simulations carried out on **2K** model in rather different conditions (see computational details) provide invariably the same picture: the two $K^+_{(1)}$ and $K^+_{(2)}$ ions experience a single file movement towards the channel cavity within the first 0.2 ns of simulatios. As a result, $K^+_{(1)}$ and $K^+_{(2)}$ occupied the WAT and the more intracellular crystallographic binding sites, respectively. Thus, removal of $K^+_{(3)}$ is reflected in an immediate instability of the system.

Our calculations indicate that the water molecules within the channel cavity are significantly polarized by the four pore helix dipoles. This finding is fully consistent

with a recent EPR study, which points to the discrepancies between water penetrating the channel and that in the bulk [10]; furthermore, it agrees with previous MD studies, which reveal the role of secondary structure elements for the polarization of the inner solvent on α-helix boundless ion channels [80,81,87].

Water molecules are expected to be polarized also in the presence of the physiological membrane potential. Indeed, the calculated pore helix electric field is much larger (~0.01 to ~ 0.1 V/Å, depending on the electrostatic model used) than that present in physiological conditions, where ~ 100 mV potential is applied to membranes some nm width.

Water polarization causes the formation of a large dipole **D** along the channel axis, directed towards the extracellular side (Fig. 3). D fluctuates widely because of the electric field of the positively charged, highly mobile $K^+_{(3)}$ cation.

Our MD simulations show that the K^+ ions remain in their initial sites (although they differ markedly in mobility (Fig. 1)), consistently with X-ray structural data {Doyle, Cabral J.M., et al. 1998 1 /id}, which suggests the presence of two potassium ions in the selectivity filter.

Electrostatic modeling suggests that the mechanism preventing rapid ion transport in the channel is based on the interaction between $K^+_{(2)}$ and the $K^+_{(3)}$/water system. This interaction is repulsive as **D** points towards $K^+_{(2)}$ (Fig. 3). It is very large (of the order of tens kcal/mol in a point charge model) because of the large magnitude of **D** and the large $K^+_{(2)}/K^+_{(3)}$ repulsion. Finally, it is almost constant (that is, not dependent on $K^+_{(3)}$ position) as $K^+_{(2)}/K^+_{(3)}$ and $K^+_{(2)}$/**D** interactions compete to each other during the dynamics (Fig. 4.10D): when $K^+_{(3)}$ close to the intracellular mouth, its electric field further polarize the water molecules (Fig. 4.10C(a)) and **D** is close to its maximum value ("saturation regime"). In this case, both $K^+_{(2)}$/**D** and $K^+_{(2)}/K^+_{(3)}$ interactions play a fundamental role for $K^+_{(2)}$ stabilization. In contrast, when $K^+_{(3)}$ is close to the selectivity filter, it generates a field just opposite to that induced by the pore helices: **D** is zero or even negative (Fig. 4.10C(c)). In this case, $K^+_{(2)}/K^+_{(3)}$ interaction energy is very large and it represents the essential ingredient for $K^+_{(2)}$ stabilization.

The essential role of the water/$K^+_{(3)}$ system was confirmed by simulations carried out without $K^+_{(3)}$. $K^+_{(1)}$ and $K^+_{(2)}$ do not remain in their original binding sites and have a single file movement towards the inner vestibule within few hundreds ps.

4.5 Potassium permeation through the selectivity filter

In this section we study by quantum chemical methods the intracellular motion of the K^+ ions in the selectivity filter that had been observed in the **2K** simulations described in the previous paragraph. Analysis of the electronic structure by performing single point calculations on protein conformations generated by classical MD simulations was reported in ref. [140] for a different system. The K^+-protein interactions during the K^+ translocation between one binding site and the following one are here investigated by using Density Functional Theory (§ 2.3, § 3.2.2) on a reduced molecular model (§ 3.1 and Fig. 3.3).

The spontaneous single file movement was caused by the removal of $K^+_{(3)}$ from the internal cavity (see previous paragraph) and occured in ≈ 60 ps. Here we focus on the structural features of the translocation of K^+ from site S1 to site S2 (frames *f0-f10* in Fig. 4.11A). The metal ion bound to backbone carbonyls of the four subunits and to water molecules WAT1 and WAT2.

In the initial configurations (*f0,f1*), the potassium ion was located in binding site S1 (Fig. 4.11A). The metal ion was coordinated by the four Tyr78 and the four Gly77 backbone carbonyls in a distorted antiprismatic geometry (Fig. 4.11B, upper sketch). The coordination number is maximum (Fig. 4.11D, left panel), and, as a consequence, the K-O distance was large (Fig. 4.11D, right panel). The interaction with second-shell ligands (Val76 and WAT1) was weak: it ranges from 4.4 to 5.3 Å.

In few ps the metal ion abandoned site S1 (frames *f2-f4).* In this process, it started losing its coordination with Tyr78 and it bound to Gly77 and WAT2. At the transition state (TS) (*f5*), it bound tightly to the four Gly77 and WAT2, and weakly to backbone oxygens belonging to Val76 and Tyr78. The polyhedron geometry can be described as a highly distorted pyramidate triangular prism (Fig. 4.11B, lower sketch). K^+ coordination number and the K-O distances reached their minimum (Fig. 4.11D). As K^+ first-shell

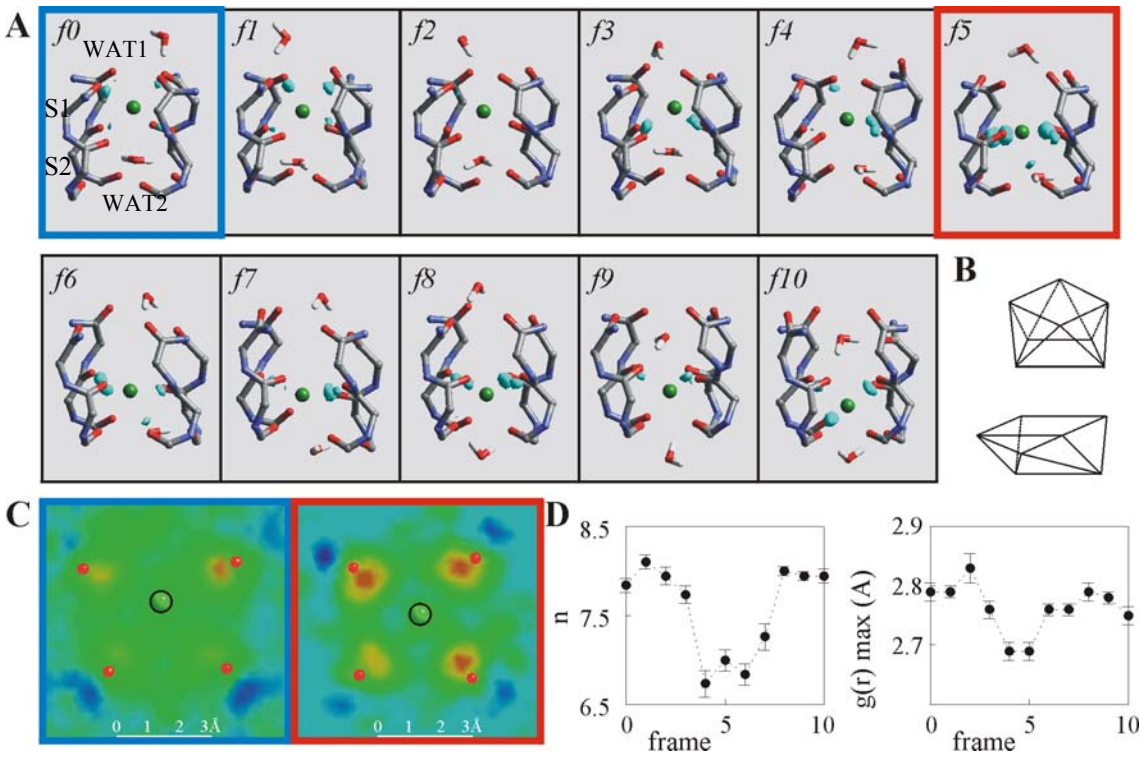

Fig. 4.11 K^+ permeation through the selectivity filter. (A) Eleven snapshots (taken each 5.7 ps) from the MD simulation [131]. The difference electron density Δρ is superimposed to the molecular structure in light blue color (the contour level 0.0202 e/Å^3); (B) Geometry of the potassium coordination polyhedra. At the binding site (frame *f0*) the metal ion is 8-coordinated with antiprismatic geometry (upper sketch). At the TS (frame *f5*), only 7 ligands bind to the K^+ and the geometry is pyramidate triangular prismatic (lower sketch); (C) Δρ of frames *f0* and *f5* is projected on a best fit plane containing K^+ ion and the four donor atoms which are mostly polarized (two Tyr78 oxygens and two Gly77 oxygens for frame *f0*, four Gly77 oxtgens for frame *f5*). Δρ ranges from blue (-0.0135 e/Å^3) to red (0.0304 e/Å^3); (D) K^+ coordination number. The maximum of its radial distribution function [$g(r_{K^+\text{-}O})$] (left) and its integral (the coordination number *n*) is plotted as a function of the frames *f0-f10*.

coordination number was smaller than in initial configurations (Fig. 4.11D), the interaction with the second-shell ligands (Val76 and Tyr78) became significant as evidenced by the second maximum of the radial distribution function (Fig. 4.12A).

Around the TS (frames *f4-f7*) WAT2 remained bound to K^+. In contrast, WAT1 did not participate to the ligand exchange process and it followed the ionic intracellular movement with some delay leaving S1 unoccupied (frames *f5-f8*). Finally, the ion

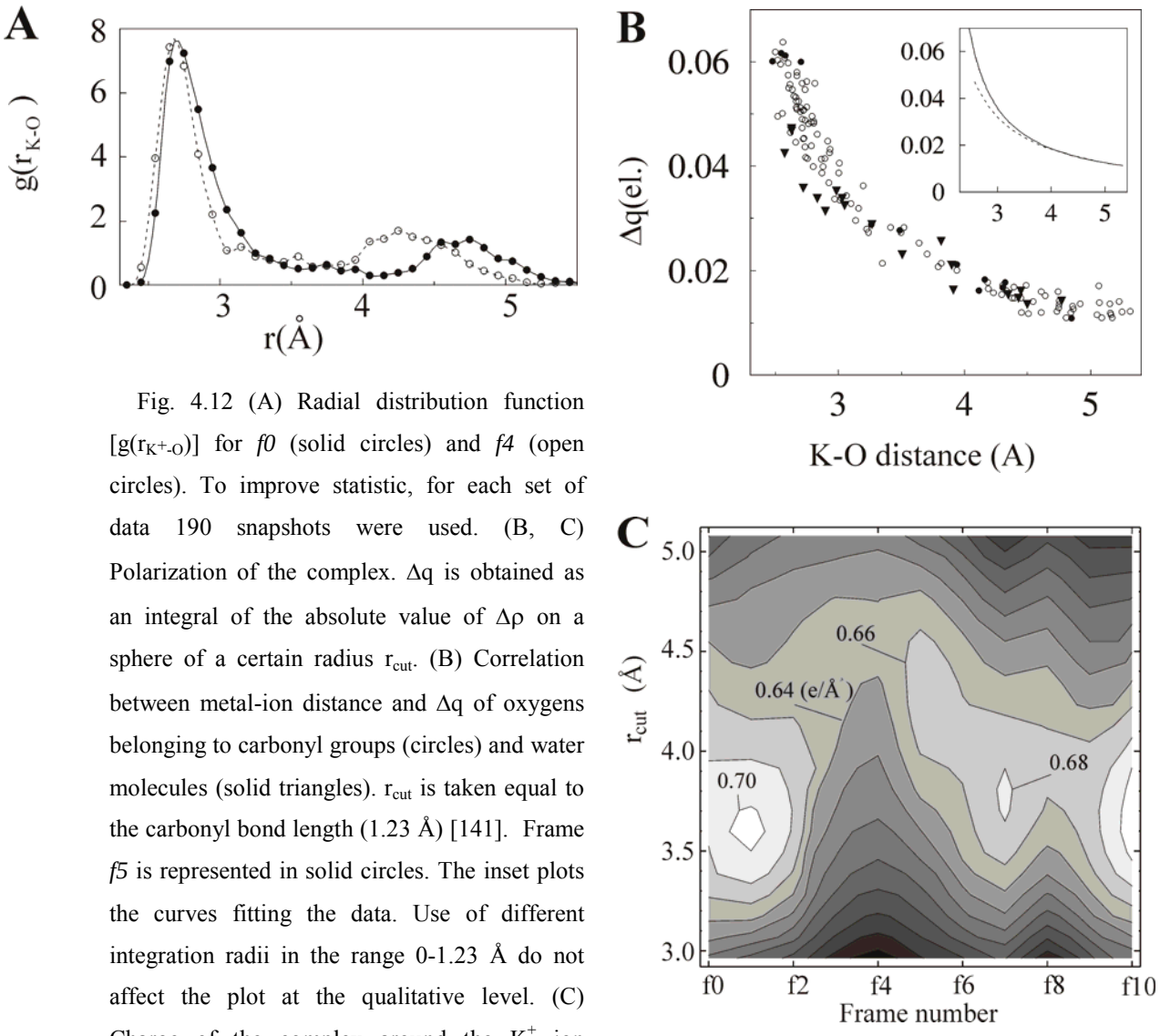

Fig. 4.12 (A) Radial distribution function [$g(r_{K^+-O})$] for *f0* (solid circles) and *f4* (open circles). To improve statistic, for each set of data 190 snapshots were used. (B, C) Polarization of the complex. Δq is obtained as an integral of the absolute value of Δρ on a sphere of a certain radius r_{cut}. (B) Correlation between metal-ion distance and Δq of oxygens belonging to carbonyl groups (circles) and water molecules (solid triangles). r_{cut} is taken equal to the carbonyl bond length (1.23 Å) [141]. Frame *f5* is represented in solid circles. The inset plots the curves fitting the data. Use of different integration radii in the range 0-1.23 Å do not affect the plot at the qualitative level. (C) Charge of the complex around the K^+ ion contoured as a function of the frame number and of the cutoff integration radius r_{cut}.

reached site S2 (*f9-f10*), previously occupied by WAT2, again characterized by a large coordination number. In S2 the ion bound exclusively to Gly77 and Val76, while both water molecules were H-bonding to carbonyls, without participating as ligands.

Polarization effects. The difference electron density Δρ (calculated here within the DFT approach) describes the rearrangement of the electronic density upon K^+ binding to the protein. Polarization effects were clearly operative and involved the carbonyl oxygen donor atoms. Interestingly, polarization *increased* on K^+ passing from the

binding site to TS (Fig. 4.11C). This is a consequence of the decrease of the K-O distance on passing from *f0* to *f5*.

Fig. 4.12B shows that this is actually a general trend of the simulation. The charge rearrangement on ligand oxygens induced by the metal ion (Δq) is indeed correlated to the K^+-O distance (Fig. 4.12A): decreasing the metal-donor distance caused an increase of the polarization. The figure furthermore suggests that polarization effects are still present at relatively large distances (5-6 Å) and that these are more significant for carbonyl groups than for water. Thus, we conclude that as expected the carbonyl oxygens are more polarizable than the water molecules and that (Fig. 4.11C,D) polarization decreased with the number of ligands.

As Δq depends crucially on the integration radius (r_{cut}), a plot of Δq as a function of r_{cut} and the frame number is of interest (Fig. 4.12C). The figure shows that initial (*f0*) and final (*f10*) ground states exhibit a similar Δq. In particular, in both cases Δq is maximum (≈ 0.7 electrons) for r_{cut} ≈ 3.7 Å, that is the first minimum in r_{K^+-O} (Fig. 4.12C). At the TS the maximum polarization is shifted to larger r_{cut} values. That is, the contribution of the second-shell ligands (Val76 and Thyr78) to the potassium chemistry becomes significant as shown already in our geometrical analysis above (Fig. 4.12A).

The electronic structure. The Wannier orbitals are obtained from the Kohn-Sham orbitals with an unitary transformation [115]. The centers of these orbitals provide a vivid representation of chemical concepts such as a covalent bond and electron lone pairs[115]. Here we focus on the centers of the oxygen donor atoms (W in Fig. 4.13A), which represent the two electron lone pairs. In particular, we are interested in the *displacement* of the centers (Fig. 4.13A) upon potassium binding to the protein [142].

Fig. 4.13B,C plot the average displacements both in terms of distance from the oxygen atoms Δ(d(O-W)) and angle with the carbonyl group Δ(∠(C-O-W)).

The displacement of the lone pairs of Val 76 (Tyr78) increased (decreased) significantly during the dynamics. Indeed, on passing from S1 to S2, K^+ exchanged Tyr78 carbonyl with that of Val76. Thus, d(K^+-O(Val76)) decreased (Fig. 2A) and consequently K^+ increasingly polarized Val78 oxygen's lone pairs. In contrast, d(K^+-O(Tyr78)) decreased and the metal ion no longer polarized Tyr78 lone pairs, becoming insensitive to the ion presence (triangles). The displacement experienced in the radial

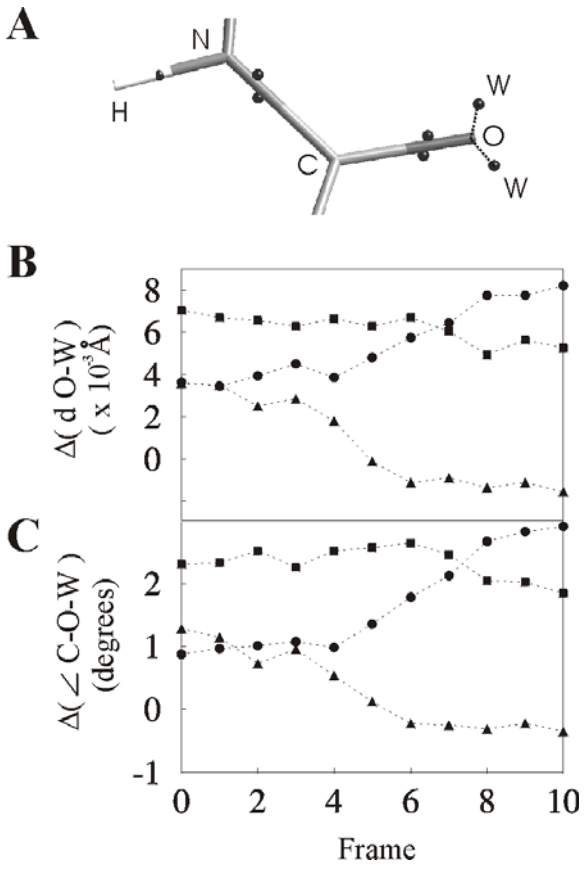

Fig. 4.13 Chemistry of carbonyl oxygens binding to potassium. (A) The Wannier centers (W) visualize the oxygen donors' lone pairs; The displacement of the W centers upon K^+ binding to the protein are reported in terms of O-W distance (B) and of C-O-W angle (C). Data for Val76, Gly77 and Tyr78 are plotted as circles, squares and triangles.

direction (~0.005 Å) is about the half than the angular one (~0.01 Å), indicating that the carbonylic oxygen's lone pairs are more easily bent than stretched.

Finally, the lone pairs of Gly77 oxygen did not change significantly during the dynamics, because they always bound the cation.

This study provides the first detailed description of the coordination chemistry of the potassium ion during the permeation process. The calculations indicate that binding sites S1 and S2 are similar coordination polyehdra to that found in the X-ray structure, i.e. an antiprismatic octaedron [8]. Passing from S1 to S2, the exchange ligands reaction of K^+ is accompanied by one water molecule (WAT2) that participates to the binding. In the transition state between the two binding sites the ion coordination polyedra changes to pyramidate triangular prism, the coordination number lowering to about seven.

The polarization effect of the K^+ ion is remarkably significant on the oxygen ligands and seems to be stronger on the carbonyl group that on the water. The effect of the potassium binding on the protein oxygens is not limited to a polarization effect, but it

also involves changes in electronic structure as evinced by analysis of the Wannier Centers geometry.

4.6 A survey of the theoretical works

Our studies [130-132] are among the first molecular dynamics approaches to the potassium channel. In this section we report an overview of the other theoretical works that appeared in these two years as well as a comparison with our data.

4.6.1 Other works on the KcsA channel (1999-2000)

The presence of one alkali ion has been detected by X-ray as a diffuse density around the middle of the cavity. The electrostatic stabilization of monovalent cations has been linked to the presence of the pore helices [8,44]. The four secondary structure elements, indeed, point with the negative side of their electric dipoles towards the cavity center, lowering the potential energy of positively charged ions at the membrane center. Electrostatic calculations [44] suggested that the stabilization is able to compensate for the free-energy loss due to the dielectric barrier found by the ions in the more hydrophobic environment of the internal cavity. Furthermore, it turned out that the protein electric field is tuned to preferentially stabilized monovalent against multivalent cations in the middle of the membrane [44].

MD simulations and Brownian Dynamics study based on simplified models of the KcsA structure have been performed by Allen *et al.* And by Chung *et al.* [143,144]. The models included only the 5 residues of the selectivity filters (from Thr75 to Gly79), K^+ ions, and water molecules. The rest of the channel pore was modeled as an hydrophobic wall and by fixed electric dipoles. From the MD simulations it appears that the two-ion configuration is the most stable, while the three ion configuration is only an intermediate state during ion transport [143].

Shrivastava and Sansom reported simulations of KcsA channel embedded in a phospholipid bilayer in different ionic occupancy [72]. Starting from a three-ion configuration (two in the filter and the third into the cavity), they observed in the simulation a concerted movement of the ions, as a consequence of ‘breathing’ motions

of the protein. The cavity ion left the internal chamber via its intracellular side, and the ions into the filter underwent a shift in the same direction. The simulation showed a single file behavior of the ion and the water molecules into the filter.

The selectivity filter loading states were extensively investigated by Åqvist and Luzhkov in a KcsA model immersed in a cylindrical slab of hydrocarbon-like atoms [71]. Using MD free energy perturbation calculations they compared simulations containing zero up to four K^+ ions in the four crystallographic binding sites. The most favored conduction pathway was found to involve only two states, with a free energy difference of about 5 kcal mol^{-1}. Both states include the cavity ion, while the ions in the filter are occupied the odd and even binding sites respectively. Free energies have been obtained through K^+ into Na^+ transformations in the two lower multi-ion states identified in the permeation pathway. The permeability ratio had been estimated 10^2-10^3 [71].

Bernèche and Roux studied the KcsA K^+ channel in a bilayer membrane [70]. Simulations with more than one water molecule per binding site led to water expulsion, supporting the view of an alternating ion-water-ion queue into the selectivity filter. They observed a concerted dynamical transition of the three ions into the pore. The cavity ion shifted to $K^+_{(3)}$ binding site with consequent single-file movements of the two ions into the filter towards the extracellular side. The final ionic configuration contains three ions into the selectivity filter.

4.6.2 Comparison with the present work

The results from Roux and Mackinnon [44] are in agreement with the polarization effect of the internal water molecules that we have recognized to be induced by the pore helix orientation. However, it appears that water has a lower dielectric constant that in bulk.

In the ns simulations cited of the KcsA [70,72], single file movements in the selectivity filters occurred in short time (< 0.5 ns), and in opposite directions. In our **3K** simulations the three ions are stable and their dynamics fairly reproduced the crystallographic data. Our systems became unstable where the presence of the cavity ion $K^+_{(3)}$ were missing. Departure of the $K^+_{(3)}$ ion from the central cavity to its intracellular

mouth (for instance as a consequence of a "breathing" motion of the channel [72]) may be a basic feature of channel gating. The present mechanism is at the speculative level, yet it is encouraging that, in the MD simulation from Shrivastava and Sansom [72] the exit of a potassium upon enlargement of the intracellular mouth triggers ion transport through the channel [72].

The work from Bernèche and Roux found a stable three-ion configuration that is very close to that we have reported by us in § 4.3.2. Both simulations, although based on different force field and carried out in different membrane environments, provide a strong suggestion that three ions may actually accommodate into the selectivity filter, occupying a fifth non-crystallographic binding site. Therefore, this ionic configuration should be taken into account as a possible state in the ion permeation pathway. An extension to the five binding sites case of the ion permeation mechanism proposed by Åqvist and Luzhkov [71] should be considered to explore the full complexity of the selectivity filter loading states.

Conclusions and perspectives

This work represents one of the first attempts to model with force field methods and *ab initio* calculations the potassium channel. From these simulations several conclusions can be drawn on both structural and functional aspects of ion permeation through the KcsA channel. The high homology between KcsA and eukaryotic voltage-gated channels may extend the domain of our conclusions to this important class of channels [43].

In the following, we report the conclusions that our calculations have provided in addressing the four issues proposed in the introduction to this thesis.

1. The overall structure of the wild-type KcsA molecular models is found to be stable in the membrane-model environment in the ns time scale. The ionic positions observed in the crystal are well reproduced by a simulation performed with three ions into the pore. The location of the n-octane/water interfaces along the TM helices turned out to be in agreement with subsequent work EPR data [10]. The comparison between wild-type and mutant simulations reveal a novel role of Asp80 (usually assumed to be an external binding site) through forming salt bridges with Arg89. The salt bridges contribute largely to the stability of the tetrameric complex.
2. The channel is engineered so as to repel anions and attract cations, i.e. K^+ and Na^+, into the first binding site within the pore. This valence selectivity in an electrically neutral channel is achieved by the specific channel conformation, with negative charges located near to the channel axis.

   When the external binding site is not yet occupied by a cation, the charge configuration of the KcsA channel is able to strip most of water molecules from a hydrated cation, thus efficiently catalyzing dehydration. As a consequence, the

rate limiting process requiring thermal activation may be the removal of the potassium from the binding sites. The calculated time-scale of the dehydration process of K^+ –few ten ps– is fully consistent with available experimental data: indeed, quasi-elastic neutron scattering measurements [56,145] established that the residence time of water molecules bound to K^+ in aqueous solution is not greater than 100 ps. Thus, the dehydration step does not seem to be an energy barrier for ion permeation.

Na^+ ion, initially located in the outer mouth, experienced a similar attraction and dehydration process. A major difference between Na^+ and K^+ in the channel pore is that Na^+ keeps more water molecules attached than K^+; this fact could be a key ingredient for ionic selectivity [64].

3. The water and K^+ dynamics have been investigated in a simulation performed with three ions into the pore. The protein polarizes water molecules inside the channel cavity, thus inducing a large electric dipole moment. This dipole and the positively charged potassium ion inside the cavity stabilize the two ions in the binding sites (and thus inhibiting ion transport) in a concerted and dynamical mechanism. This effect occurred despite the rather large distance between the cavity and the ions into the filter. These simulations show that the concept of single file transport may be extended beyond the selectivity filter, involving also the ion into the cavity. This result, together with those from Shrivastava and Sansom [72], provides a plausible picture of the mechanisms underlying the ion triggering of the intracellular gate of the channel. Because solvent continuum models cannot describe this mechanism, explicit treatment of the solvent appears necessary to describe correctly the biological properties of the channel.
4. The ion translocation through the selectivity filter was studied by MD and DFT methods. Structural and quantum chemical studies during the single file movements provide information on the coordination chemistry of the K^+ ions into the selectivity filter. The coordination number at the transition state is lower than that of the binding sites. At the transition state the ion coordination number has been found to be lower than in the binding sites and a different coordination polyedra is present (i.e. pyramidate triangular prism instead that antiprismatic

octahedron). K^+ ion polarizes the ligand oxygens of water, and, more, of the carbonyl group. The presence of the ion affects the electronic structure, as showed by a shift of the centers of the maximally localized Wannier centers.

At the speculation level, sodium may involve higher polarization on the surrounding oxygens, and probably may enter the filter with more hydration molecules [1,64,130]. Differences in the ligand geometry of the transition state as well as in the protein and water polarization could have a key role in the ionic selectivity.

In conclusion, our calculations points out the crucial role of water for a variety of processes. Water seems to be an essential ingredient for the cation coordination during the binding, for the single file behavior into the selectivity filter, and to trigger the dynamics of the permeating ions.

Our results provide a perspective for future theoretical studies of ionic selectivity and K^+ permeation mechanisms. The rate limiting step to ion transport has to be found in the K^+ translocation into the selectivity filter and not, as in gramicidin [1], in the ion dehydration process. Further studies could be addressed to the investigation of the exact location of the highest free energy barrier, probably located between two binding sites of the filter. The analysis we made on the geometrical and quantum chemical characterization along the single file movements may be extended to the full selectivity filter pathway, and enriched with the use of free energy perturbation techniques or enhanced sampling methods [89,146].

For an accurate description of the permeation, the full dynamics of the ion translocation could be performed using *ab initio* methods for both Na^+ and K^+ ions. Quantum Mechanics/Molecular Dynamics methods are the best candidates for this investigation, allowing to include the full chemistry of the ligands (i.e. our reduced model) without neglecting the effect of the whole protein [147].

Acknowledgements

I gratefully thank my supervisors, Paolo Carloni and Vincent Torre, who introduced me to theoretical and experimental biochemistry and biophysics.

I wish to thank Roderick MacKinnon for providing us with the coordinates of the KcsA channel before the PDB deposition; Joao Cabral, Eduardo Perozo, and Luis Cuello for useful discussions.

Thanks to Doriano Lamba for having answering all my questions about X-ray crystallography and for many useful discussions.

I am with great debit to Paul Tangney: whithout her prezious and unsubstituible helps, thes tesis whould cointains very much more english error than thoose it actually contained as a matter of fact.

… ok, I'll switch to italian.

Un grazie speciale a Silvia, per essermi stata sempre vicinissima in tutti questi anni nonostante la lontananza.

Grazie a mia mamma Angela per avermi sempre incoraggiato e creduto in me. Grazie a Daniele perche' su di lui ho potuto sempre contare e per riuscire a trovare sempre il momento giusto per fare un paio di giri a Monaco.

Grazie a Federico per non aver mai lesinato sulla quantita' di cavolfiori e peperoni che hanno da sempre abitato il nostro frigorifero e ad Antonio per le sue doti da sommelier. Sono indubbiamente i compagni di casa ideali.

Un grazie a Francio e a Guido, che rimangono sempre due amici insostituibili.

Grazie anche a Lorenzo, utile fonte di saggezza, ad Alessandro con il quale mi aspetteranno interminabili passeggiate, a Gabriele, insuperabile nel pollo al curry, al mitico Gianluca, all'imprevedibile Andrea, al saggio Mario ed alla saggia Valeria.

Grazie a tutti coloro che mi hanno aiutato a non sentirmi mai solo nella room 26: Sergio, Stefano, Lore, Francesco, Valeria, Marco, Andrea, Gianni, Ansgar, Frank, Matteo, David, Francesco…e moltissimi altri…

Grazie a Giovanni per avermi fatto sempre sentire a casa nel suo ufficio (non so se sara' felice di cio') e per i suoi preziosi consigli. Grazie a Giuseppe, a Sandro, ad Alberto, a Luca e a Massimo per tutto il tempo passato insieme.

Un ringraziamento particolare va a tutti quelli che mi sono dimenticato… e sono tanti.

Io credo invece di meritare il ringraziamento delle ferrovie dello Stato per aver sempre riservato una cospicua parte del mio stipendio all'acquisto di biglietti del treno.

Bibliography

[1] B. Hille, Ionic channels of excitable membranes, Sinauer associates, 1992.

[2] Ionic channels, New York 1988.

[3] Catterall W.A., Structure and function of voltage-gated ion channels. *Annu. Rev. Biochem.* 64, 493-531 (1995).

[4] Jan L.Y. and Jan Y.N., Cloned potassium channels from eukariotes and prokariotes. *Annu. Rev. Neurosci.* 20, 91-123 (1997).

[5] Hille B. and Schwartz W.J., Potassium channels as multi-ion single-files pores. *J. Gen. Physiol.* 72, 409-442 (1978).

[6] C. Branden and J. Tooze , Introduction to protein structure, p. -410, 1999.

[7] Roux B.K.M., Ion transport in a model gramicidin channel. *Biophys. J.* 59, 961-981 (1991).

[8] Doyle D.A., Cabral J.M., Pfuetzner R.A., Kuo A., Gulbis J.M., Cohen S.L., Chait B.T. and MacKinnon R., The structure of the potassium channel: molecular basis of K+ conduction and selectivity. *Science* 280, 69-77 (1998).

[9] Perozo E., Cortes D.M. and Cuello L.G., Structural rearrangements underlying K+-channel activation gating. *Science* 285, 73-78 (1999).

[10] Gross A., Columbus L., Hideg K., Altenbach C. and Hubbell W.L., Structure of the KcsA potassium channel from Streptomyces lividans: a site-directed spin labeling study of the second transmembrane segment. *Biochemistry* 38, 10324-10335 (1999).

[11] Sansom M.S., Smith G.R., Adcock C. and Biggin P.C., The dielectric properties of water within model transbilayer pores. *Biophys. J.* 73, 2404-2415 (1997).

[12] B. Alberts, D. Bray, J. Lewis, N. Raff, K. Roberts and J. D. Watson, Molecular biology of the cell, Garland Publishing, New York 1995.

[13] H. Lodish, D. Baltimore, A. Berk, S. L. Zipursky, P. Matsudaira and J. Darnell, Molecular cell biology, Scientifica American Books, New York 1995.

[14] Chang G., Spencer R.H., Lee A.T., Barclay M.T. and Rees D.C., Structure of the MscL Homolog from mycobacterium tuberculosis: a gated mechanosensitive ion channel. *Science* 282, 2220-2226 (1998).

[15] Zagotta W.N. and Siegelbaum S.A., Structure and function of cyclic nucleotide-gated channels. *Annu. Rev. Neurosci.* 19, 235-263 (1996).

[16] Schrempf H., Schmidt O., Kummerlen R., Hinnah S., Muller D., Betzler M., Steinkamp T. and Wagner R., A prokariotic potassium ion channel with two predicted transmembrane segments from Streptomyces lividans. *Embo J.* 14, 5170-5178 (1995).

[17] Cuello L., Romero J.G., Cortes D.M. and Perozo E., pH-dependent gating in the Streptomyces lividans K+ channel. *Biochemistry* 37, 3229-3236 (1998).

[18] Jentsch T.J., Gunther W., Pusch M. and Schwappach B., Properties of voltage-gated chloride channels of the ClC gene family. *J. Physiol (Lond)* 482, 19S-25S (1995).

[19] Sheppard D.N. and Welsh M.J., Structure and function of the CFTR chloride channel. *Physiol Rev.* 79, S23-S45 (1999).

[20] F. M. Ashcroft, Ion channels and disease, Academic Press, San Diego, Californa 2000.

[21] P. Läuger, Electrogenic ion pumps, Sinauer assiciates, 1991.

[22] Cole K.S. and Curtis H.J., Electric impedance of *Nitella* during activity. *J. Gen. Physiol.* 22, 37-64 (1938).

[23] Hodgkin A.L. and Huxley A.F., A quantitative description of membrane current ond its application to conduction and excitation in nerve. *J. Physiol.* 117, 500-544 (1952).

[24] Tempel B.L., Papazian D.M., Schwartz T.L., Jan Y.N. and Yan L.Y., Sequence of a probable potassium channel component encoded at *Shaker* locus of *Drosophila*. *Science* 237, 770-775 (1987).

[25] Wei A., Covarrubias M., Butler A., Baker K., Pak M. and Salkoff L., K^+ current diversity is produced by an extended gene family conserved in Drosophila and mouse. *Science* 248, 599-603 (1990).

[26] Shen N.V., Chen X., Boyer M.M. and Pfaffinger P.J., Deletion analysis of the K+ channel assembly. *Neuron* 11, 67-76 (1993).

[27] Kirsch G.E., Pascual J.M. and Shieh C.-C., Functional role of conserved aspartate in the external mouth of voltage-gated potassium channels. *Biophys. J.* 68, 1804-1813 (1995).

[28] Pascual J.M., Shieh C.-C., Kirsch G.E. and Brown A.M., K+ pore structure revealed by reporter cysteines at inner and outer surfaces. *Neuron* 14, 1055-1063 (1995).

[29] Heginbotham L., Lu Z., Abramson T. and MacKinnon R., Mutations in the K+ channel signature sequence. *Biophys. J.* 66, 1061-1067 (1994).

[30] Kubo Y., Yoshimichi M. and Heinemann S.H., Probing pore topology and conformational changes of Kir2.1 potassium channels by cysteine scanning mutagenesis. *Febs Lett.* 435, 69-73 (1998).

[31] MacKinnon R., Determination of the subunit stoichiometry of a voltage activated potassium channel. *Nature* 350, 232-235 (1991).

[32] Hodgkin R.D. and Keynes R.D., The potassium permeability of a giant nerve fibre. *J. Physiol.* 128, 61-88 (1955).

[33] Hagiwara S. and Takahashi K., The anomalous rectification and cation selectivity of the membrane of a starfish egg cell. *J. Memb. Biol.* 18, 61-80 (1974).

[34] Milkman R., An *Escherichia coli* analogue of eukaryotic potassium channel proteins. *Proc. Natl. Acad. Sci.* 91, 3510-3514 (1994).

[35] MacKinnon R. and Doyle D.A., Prokaryotes offer hope for potassium channel structural studies. *Nat. Struct. Biol.* 4, 879 (1997).

[36] Cortes D.M. and Perozo E., Structural dynamics of the *Streptomyces lividans* K^+ channel (SKC1): oligomeric stoichiometry and stability. *Biochemistry* 36, 10343-10352 (1997).

[37] Heginbotham L., Odessey E. and Miller C., Tetrameric stoichiometry of a prokaryotic K^+ channel. *Biochemistry* 36, 10335-10342 (1997).

[38] Heginbotham L., Kolmakova-Partensky L. and Miller C., Functional reconstruction of a prokaryotic K^+ channel. *J. Gen. Physiol.* 111, 741-749 (1998).

[39] Heginbotham L., LeMasurier M., Kolmakova-Partensky L. and Miller C., Single streptomyces lividans K(+) channels: functional asymmetries and sidedness of proton activation. *J. Gen. Physiol* 114, 551-560 (1999).

[40] Perozo E., Cortes D.M. and Cuello L., Three-dimensional architecture and gating mechanism of a K+ channel studied by EPR spettroscopy. *Nat. Struct. Biol.* 5, 459-469 (1998).

[41] Meuser D., Splitt H., Wagner R. and Schrempf H., Exploring the open pore of the potassium channel from Streptomyces lividans. *Febs Lett.* 462, 447-452 (1999).

[42] Garcia M.L., Garcia-Calvo M., Hidalgo P., Lee A. and MacKinnon R., Purification and characterization of three inhibitors of voltage- dependent K+ channels from Leiurus quinquestriatus var. hebraeus venom. *Biochemistry* 33, 6834-6839 (1994).

[43] MacKinnon R., Cohen S.L., Kuo A., Lee A. and Chait B.T., Structural conservation in prokaryotic and eukaryotic potassium channels. *Science* 280, 106-109 (1998).

[44] Roux B. and MacKinnon R., The cavity and pore helices in the KcsA K+ channel: electrostatic stabilization of monovalent cations. *Science* 285, 100-102 (1999).

[45] Armstrong C., The vision of the pore. *Science* 280, 56-57 (1998).

[46] Jiang Y. and MacKinnon R., The barium site in a potassium channel by X-ray crystallography. *J. Gen. Physiol.* 115, 269-272 (2000).

[47] C. R. Cantor and P. R. Schimmel, Biophysical chemistry, W.H. Freeman and company, San Francisco 1980.

[48] Hubbell W.L. and Altenbach C., Investigation of structure and dynamics in membrane proteins using site-directed spin labeling. *Curr. Opinion in Struct. Biol.* 4, 566-573 (1994).

[49] Durrel S.R. and Guy H.R., Structural model of the outer vestibule and selectivity filter of the Shaker voltage-gated K+ channel. *Neuropharmacology* 35, 761-773 (1996).

[50] Durrel S.R., Hao Y. and Guy H.R., Structural models in the transmembrane region of voltage-gated and other K+ channels in open, closed, and inactivated conformations. *J. Struct. Biol.* 121, 263-284 (1998).

[51] Wallace B.A., Common structural features in gramicidin and other ion channels. *Bioessays* 22, 227-234 (2000).

[52] Burkhart B.M., Li N., Langs D.A., Pangborn W.A. and Duax W.L., The conducting form of gramicidin A is a right-handed double-stranded double helix. *Proc. Natl. Acad. Sci. U. S. A* 95, 12950-12955 (1998).

[53] Ketchem R.R., Hu W. and Cross T.A., High-resolution conformation of gramicidin A in a lipid bilayer by solid-state NMR. *Science* 261, 1457-1460 (1993).

[54] Ketchem R.R., Lee K.C., Huo S. and Cross T.A., Macromolecular structural elucidation with solid-state NMR-derived orientational constraints. *J. Biomol. NMR* 8, 1-14 (1996).

[55] Cross T.A., Arseniev A., Cornell B.A., Davis J.H., Killian J.A., Koeppe R.E., Nicholson L.K., Separovic F. and Wallace B.A., Gramicidin channel controversy--revisited [comment]. *Nat. Struct. Biol.* 6, 610-611 (1999).

[56] Ohtaki H. and Radnai T., Structure and dynamics of hydrated ios. *Chem. Rev.* 93, 1157-1204 (1993).

[57] Partenskii M.B. and Jordan P.C., Theoretical perspectives on ion-channel electrostatics: continuum and microscopic approaches. *Q. Rev. Biophys.* 25, 477-510 (1992).

[58] Eisenman G., Cation selective electrodes and their mode of rectification. *Biophys. J.* 2, 259-323 (1962).

[59] Eisenman G., The influence of Na, K, Li, Rb, and Cs on cellular potentials and related phenomena. *Bol. Inst. Estud. Med. Biol.* 21, 155-183 (1963).

[60] Born M., Volumen und Hydratationswärme der Ionen. *Z. Phys.* 1, 45-48 (1920).

[61] Chiamvimonvat N., Perez-Garcia M.T., Tomaselli G.F. and Marban E., Control of ion flux and selectivity by negatively charged residues in the outer mouth of rat sodium channels. *J. Physiol (Lond)* 491 (Pt 1), 51-59 (1996).

[62] Favre I., Moczydlowski E. and Schild L., On the structural basis for ionic selectivity among Na^+, K^+, and Ca^{2+} in the voltage-gated sodium channel. *Biophys. J.* 71 , 3110-3125 (1996).

[63] Fuller C.M., Berdiev B.K., Shlyonsky V.G., Ismailov I.I. and Benos D.J., Point mutations in alpha bENaC regulate channel gating, ion selectivity, and sensitivity to amiloride. *Biophys. J.* 72, 1622-1632 (1997).

[64] Laio A. and Torre V., Physical origin of selectivity in ionic channels of biological membranes. *Biophys. J.* 76, 129-148 (1999).

[65] Roux B., Valence selectivity of the gramicidin channel: a Molecular Dynamics free energy perturbation study. *Biophys. J.* 71, 3177-3185 (1996).

[66] Roux B. and Karplus M., Ion transport in the gramicidin channel: free energy of the solvated right-handed dimer in a model membrane. *J. Am. Chem. Soc.* 115, 3250-3262 (1993).

[67] Roux B. and Carplus M., Molecular dynamics simulations of the gramicidin channel. *Annu. Rev. Biophys. Biomol. Struct.* 23, 731-761 (1994).

[68] Dorman D., Partenskii M.B. and Jordan P.C., A semi-microscopic Monte Carlo study of permeation energetics in a gramicidin-like channel. *Biophys. J.* 70, 121-134 (1996).

[69] Sagnella D.E., Laasonen K. and Klein M.L., Ab initio Molecular Dynamics study of proton transfer in a poliglycine analog of the ion channel gramicidin A. *Biophys. J.* 71, 1172-1178 (1996).

[70] Berneche S. and Roux B., Molecular dynamics of the KcsA K(+) channel in a bilayer membrane. *Biophys. J* 78, 2900-2917 (2000).

[71] Aqvist J. and Luzhkov V., Ion permeation mechanism of the potassium channel. *Nature* 404, 881-884 (2000).

[72] Shrivastava I.H. and Sansom M.S., Simulations of Ion Permeation Through a Potassium Channel: Molecular Dynamics of KcsA in a Phospholipid Bilayer. *Biophys. J* 78, 557-570 (2000).

[73] Granick S., Motions and relaxations of confined liquids. *Science* 253, 1374-1379 (1991).

[74] Silvestrelli P.L. and Parrinello M., Water molecule dipole in the gas and in the liquid phase. *Phys. Rev. Lett.* 82, 3308-3311 (1999).

[75] Silvestrelli P.L. and Parrinello M., Structural, electronic, and bonding properties of liquid water from first principles. *J. Chem. Phys.* 111, 3572-3580 (1999).

[76] Partenskii M.B. and Jordan P.C., Nonlinear dielectric behavior of water in transmembrane ion channels: ion energy barriers and the channel dielectric constant. *J. Phys. Chem.* 96, 3906-3910 (1992).

[77] Sancho M., Partenskii M.B., Dorman V. and Jordan P.C., Extended dipolar chain model for ion channels: electrostriction effects and the translocational energy barrier. *Biophys. J.* 68, 427-433 (1995).

[78] Cheng W., Wang C.X., Chen W.Z., Xu Y.W. and Shi Y.Y., Investigating the dielectric effects of channel pore water on the electrostatic barriers of the permeation ion by the finite difference Poisson-Boltzmann method. *Eur. Biophys. J.* 27, 105-112 (1998).

[79] Hartnig C., Witschel W. and Spohr E., Molecular dynamics study of the structure and dynamics of water in cylindrical pores. *J. Phys. Chem* 102, 1241-1249 (1998).

[80] Breed J., Sankararamakrish R., Kerr I.D. and Sansom M.S.P., Molecular Dynamics simulations of water within models of ion channels. *Biophys. J.* 70, 1643-1661 (1996).

[81] Smith G.R. and Sansom M.S.P., Dynamic properties of Na^+ ions in models of ion channels: a molecular dynamics study. *Biophys. J.* 75, 2767-2782 (1998).

[82] Zhong Q., Jiang Q., Moore P.B., Newns D.M. and Klein M.L., Molecular Dynamics simulation of a synthetic ion channel. *Biophys. J.* 74, 3-10 (1998).

[83] Zhong Q., Moore P.B., Newns D.M. and Klein M.L., Molecular dynamics study of the LS3 voltage-gated ion channel. *FEBS Lett* 427, 267-270 (1998).

[84] Moore P.B., Zhong Q., Husslein T. and Klein M.L., Simulation of the HIV-1 Vpu transmembrane domain as a pentameric bundle. *FEBS Lett* 431, 143-148 (1998).

[85] Zhong Q., Husslein T., Moore P.B., Newns D.M., Pattnaik P. and Klein M.L., The M2 channel of influenza A virus: a molecular dynamics study. *FEBS Lett* 434, 265-271 (1998).

[86] Dieckmann G.R., Lear J.D.Z.Q., Klein M.L., DeGrado W.F. and Sharp K.A., Exploration of the structural features defining the conduction properties of a synthetic ion channel. *Biophys. J.* 76, 618-630 (1999).

[87] Tieleman D.P., Berendsen H.J. and Sansom M.S., An alamethicin channel in a lipid bilayer: molecular dynamics simulations. *Biophys. J* 76, 1757-1769 (1999).

[88] Randa H.S., Forrest L.R., Voth G.A. and Sansom M.S., Molecular dynamics of synthetic leucine-serine ion channels in a phospholipid membrane. *Biophys. J.* 77, 2400-2410 (1999).

[89] M. P. Allen and D. J. Tildesley, Computer Simulation of Liquids, Oxford University Press, New York 1987.

[90] A. R. Leach, Molecular modelling. Principles and applications, Addison Wesley, Singapore 1996.

[91] R. G. Parr and W. Yang, Density-Functional theory of atoms and molecules, Oxford University Press, New York 1989.

[92] Cornell W.D., Cieplack P., Bayly C.I., Gould I.R., Merz K.M., Ferguson D.M., Spellmeyer D.C., Fox T. and Ca, A second generation force field for the simulation of proteins, nucleic acids, and organic molecules. *J. Am. Chem. Soc.* 117, 5179-5197 (1995).

[93] Bayly C., Cieplack P., Cornell W. and Kollman P.A., A well-behaved electrostatic potential based method using charge restraints deriving atomic charges: the RESP model. *J. Phys. Chem.* 97, 10269-10280 (1993).

[94] Singh U.C. and Kollman P.A., *J. Comp. Chem.* 5, 129 (1984).

[95] Swope W.C., Anderson H.C., Berens P.H. and Wilson K.R., A computer simulation method for the calculation of equilibrium constants for the formation of physical clusters of molecules: application to small water clusters. *J. Chem. Phys.* 76, 637-649 (2000).

[96] Ryckaert J.-P., Ciccotti G. and Berendsen H.J.C., Numerical integration of the cartesian equations of motion of a system with constraints: Molecular Dynamics of n-alkanes. *J. Comp. Phys.* 23, 327-341 (1977).

[97] Berendsen H.J.C., Postma J.P.M., van Gunsteren W.F., Di Nola A. and Haak J.R., *J. Chem. Phys.* 81, 3684-3690 (1984).

[98] Darden T., York D. and Pedersen L., Particle mesh Ewald: an N log(N) method for Ewald sums in large systems. *J. Chem. Phys.* 98, 10089-10092 (1993).

[99] Essman U., Perera L., Berkowitz M.L., Darden T., Lee H. and Pedersen L.G., A smooth particle mesh Ewald method. *J. Chem. Phys. B* 103, 8577-8593 (1995).

[100] McLachlan A.D., Gene duplications in the structural evolution of chymotrypsin. *J. Mol. Biol.* 128, 49-79 (1979).

[101] Honig B. and Nicholls A., Classical electrostatic in biology and chemistry. *Science* 268, 1144-1149 (1995).

[102] Gilson M.K., Sharp K.A. and Honig B.H., Calculating the electrostatic potential of molecules in solution: method and error assessment. *J. Comp. Chem.* 9, 327-335 (1987).

[103] Bruccoleri R.E., Novotny J. and Davis M.E., Finite difference Poison-Boltzmann electrostatic calculations: increased accuracy achieved by armonic dielectric smoothing and charge antialiasing. *J. Comp. Chem.* 18, 268-276 (1997).

[104] Hohenberg P. and Kohn W., Inhomogeneous electron gas. *Phys. Rev.* 136, B864-B871 (1964).

[105] Kohn W. and Sham L.J., Self-consistent equations including exchange and correlation effects. *Phys. Rev.* 140, A1133-A1138 (1965).

[106] Ceperley D.M. and Alder B.J., Ground-state of the electron gas by a stochastic method. *Phys. Rev. Lett.* 45, 566-569 (1980).

[107] Becke A.D., Density-functional exchange-energy approximation with the correct asymptotic behaviour. *Phys. Rev. A* 38, 3098-3100 (1988).

[108] Lee C.L., Yang W. and Parr R.G., Development of the Colle-Salvetti correlation-energy formula into a functional of the electron density. *Phys. Rev. B* 37, 785-789 (1988).

[109] Colle R. and Salvetti D., *Theor. Chim. Acta* 37, 329 (1975).

[110] Barnett R.N. and Landman U., Born-Oppenheimer molecular dynamics simulations of finite systems: structure and dynamics of $(H_2O)^2$. *Phys. Rev. B* 48, 2081-2097 (1993).

[111] Kerker G.P., *J. Phys. C* 13, L189 (1980).

[112] Bachelet G.B., Hamann D.R. and Schlüter M., *Phys. Rev. B* 26, 4199 (1982).

[113] Vanderbilt D., Optimally smooth norm-conserving pseudopotentials. *Phys. Rev. B* 32, 8412 (1985).

[114] Troullier N. and Martins J.L., Efficient pseudopotentials for plane-wave calculations. *Phys. Rev. B* 43, 1993-2006 (1991).

[115] Marzari N. and Vanderbilt D., Maximally localized generalized Wannier functions for composite energy bands. *Phys. Rev. B* 56, 12847-12865 (1997).

[116] L. Pauling, General Chemistry, Dover Publications Inc., New York 1988.

[117] Alber F., Folkers G. and Carloni P., Dimethyl phosphate: stereoelectronic versus enviroment effect. *J. Phys. Chem. B* 103, 6121-6126 (1999).

[118] Gouaux E., Single potassium ion seek open channel for transmembrane travels: teles from the KcsA structure. *Structure* 6, 1221-1226 (1998).

[119] Case D.A., Pearlman D.A., Caldwell J.W., Cheatham III T.E., Ross W.S., Simmerling C.L., Darden T.A., Merz K.M., Stanton R.V., Cheng A.L., Vincent

J.J., Crowley M., Ferguson D.M., Radmer R.J., Seibel G.L., Singh U.C., Weiner P.K. and Kollman P.A., Amber 5. *University of California, San Francisco* (1997).

[120] Aqvist J., Ion-water interaction potentials derived from free energy perturbation simulations. *J. Phys. Chem.* 94, 8021-8024 (1990).

[121] Kaminski G. and Jorgensen W.L., Performance of the AMBER94, MMFF94, and OPLS-AA force fields for modeling organic liquids. *J. Phys. Chem.* 100, 18010-18013 (1996).

[122] Chen B., Martin M.G. and Siepmann J.I., Thermodynamic properties of the Williams, OPLS-AA, and MMFF94 All-Atom foce fields for normal alkanes. *J. Phys. Chem. B* 102, 2578-2586 (1998).

[123] Jorgensen W.L., Chandrasekhar J. and Madura J.D., Comparison of simple potential functions for simulating liquid water. *J. Chem. Phys.* 79, 926-935 (1983).

[124] Connolly M.L., Solvent-accessible surfaces of proteins and nucleic acids. *Science* 221, 709-713 (1983).

[125] Morris A.L., MacArthur M.W., Hutchinson E.G. and Thornton J.M., Stereochemical quality of protein structure coordinates. *Proteins* 12, 345-364 (1992).

[126] Song H.L. and Jayendran C.R., *J. Phys. Chem.* 100, 1420 (1996).

[127] Smart O.S., Neduvelil J.G., Wang X., Wallace B.A. and Sansom M.S., HOLE: a program for the analysis of the pore dimensions of ion channel structural models. *J. Mol. Graph.* 14 , 354-60, 376 (1996).

[128] Cerius2 v.3.8. *Molecular Symulations Inc.* (2000).

[129] Humphrey W., Dalke A. and Shulten K., VMD - Visual Molecular Dynamics. *J. Molec. Graphics* 14, 33-38 (1996).

[130] Guidoni L., Torre V. and Carloni P., Potassium and sodium binding to the outer mouth of the K+ channel. *Biochemistry* 38, 8599-8604 (1999).

[131] Guidoni L., Torre V. and Carloni P., Water and potassium dynamics inside the KcsA K^+ channel. *Febs Lett.* 477, 37-42 (2000).

[132] Guidoni L., Torre V. and Carloni P., Potassium permeation through the selectivity filter of the KcsA channel: a density functional study. *to be submitted to J. B. I. C.* (2000).

[133] Khodakhah K., Melishchuk A. and Armstrong C.M., Killing K channels with TEA+. *Proc. Natl. Acad. Sci. U. S. A* 94, 13335-13338 (1997).

[134] Melishchuk A., Loboda A. and Armstrong C.M., Loss of shaker K channel conductance in 0 K+ solutions: role of the voltage sensor. *Biophys. J.* 75, 1828-1835 (1998).

[135] Guidoni L., Torre V. and Carloni P., K+ - potassium channel interactions explored by molecular dynamics simulation. *Biophys. J.* 76, A153 (1999).

[136] Goldstein S.A.N., Pheasant D.J. and Miller C., The charybdotoxin receptor of a Shaker K+ channel: peptide and channel residues mediating molecular recognition. *Neuron* 12, 1377-1388 (1994).

[137] Cuello L.G. and Perozo E., A network of charges in the extracellular surface of KcsA contributes to oligomeric stability. *Biophys. J.* 78, 398A (2000).

[138] Kaminski G., Duffy E.M., Matsui T. and Jorgensen W.L., Free energies of hydration and pure liquid preperties of hydrocarbons from the OPLS all-atom model. *J. Phys. Chem.* 98, 13077-13082 (1994).

[139] Cabral J.M., *Personal communication* (2000).

[140] Nadig G., van Zant L.C., Dixon S.L. and Merz K.M., Charge-transfer interactions in macromolecular systems: a new view of protein/water interface. *J. Am. Chem. Soc.* 120, 5593-5594 (1998).

[141] Weiner S.J., Kollman P.A., Nguyen D.T. and Case D.A., *J. Comp. Chem.* 7, 230-252 (1986).

[142] Piana S. and Carloni P., Conformational flexibility of the catalytic Asp dyad in HIV-1 protease: An ab initio study on the free enzyme. *Proteins* 39, 26-36 (2000).

[143] Allen T.W., Kuyucak S. and Chung S.H., Molecular dynamics study of the KcsA potassium channel. *Biophys. J.* 77, 2502-2516 (1999).

[144] Chung S.H., Allen T.W., Hoyles M. and Kuyucak S., Permeation of ions across the potassium channel: brownian dynamics studies. *Biophys. J.* 77, 2517-2533 (1999).

[145] Friedman H.L., *Chim. Scripta* 25, 42 (1985).

[146] VandeVodele J. and Rothlisberger U., Efficient multidimensional free energy calculations for ab initio molecular dynamics using classical bias potentials. *J. Chem. Phys.* 36, 4863-4868 (2000).

[147] Rothlisberger U., Carloni P., Doclo K. and Parrinello M., A comparative study of galactose oxidase and active site analogs based on QM/MM Car-Parrinello simulations. *J. Biol. Inorg. Chem* 5, 236-250 (2000).